

1 **Increasing resolution and resolving convection improves**
2 **the simulation of cloud-radiative effects over the North**
3 **Atlantic**

4 **Fabian Senf¹, Aiko Voigt^{2,3}, Nicolas Clerboux⁴, Anja Hünerbein¹, Hartwig**
5 **Deneke¹**

6 ¹Leibniz Institute for Tropospheric Research, Leipzig

7 ²Institute for Meteorology and Climate Research - Department Troposphere Research, Karlsruhe Institute
8 of Technology, Karlsruhe

9 ³Lamont-Doherty Earth Observatory, Columbia University, New York, USA

10 ⁴Royal Meteorological Institute of Belgium, Brussels

11 **Key Points:**

- 12 • net biases in cloud-radiative effects become smaller as grid spacing is decreased
13 from 80 to 10 km
14 • at resolutions of 10 km and finer, improvements result from disabling the convec-
15 tion scheme
16 • reduced biases compensation between longwave and shortwave leads to more re-
17 alistic radiation fluxes

Corresponding author: Fabian Senf, senf@tropos.de

Abstract

Clouds interact with atmospheric radiation and substantially modify the Earth's energy budget. Cloud formation processes occur over a vast range of spatial and temporal scales which make their thorough numerical representation challenging. Therefore, the impact of parameter choices for the simulation of cloud-radiative effects is assessed in the current study. Numerical experiments were carried out using the ICON model with varying grid spacings between 2.5 and 80 km and with different subgrid-scale parameterization approaches. Simulations have been performed over the North Atlantic with either one-moment or two-moment microphysics and with convection being parameterized or explicitly resolved by grid-scale dynamics. Simulated cloud-radiative effects are compared to products derived from Meteosat measurements. Furthermore, a sophisticated cloud classification algorithm is applied to understand the differences and dependencies of simulated and observed cloud-radiative effects. The cloud classification algorithm developed for the satellite observations is also applied to the simulation output based on synthetic infrared brightness temperatures, a novel approach that guarantees a consistent and fair comparison. It is found that flux biases originate equally from clearsky and cloudy parts of the radiation field. Simulated cloud amounts and cloud-radiative effects are dominated by marine, shallow clouds, and their behaviour is highly resolution dependent. Bias compensation between shortwave and longwave flux biases, seen in the coarser simulations, is significantly diminished for higher resolutions. Based on the analysis results, it is argued that cloud-microphysical and cloud-radiative properties have to be adjusted to further improve agreement with observed cloud-radiative effects.

Plain Language Summary

Clouds are a major challenge for climate science and their effects are difficult to quantify. Clouds scatter sunlight back into space and thus prevent the Earth from warming up. But clouds also hold back heat radiation upwelling from the surface. Both effects typically compensate each other and thus lead to the net cloud-radiative effect. Computer programs that are used to simulate the climate - so-called climate models - often use very coarse grid-box sizes in their computational mesh. Cloud processes and their effects are represented in them in a very simplified way, which leads to problems. For this reason, this study deals with the question to what extent the simulations of cloud-radiative effects can be improved by choosing more precise descriptions of the cloud processes. To investigate this, different configurations of realistic weather models were taken to simulate cloud formation over the North Atlantic. The resulting simulation data were compared to satellite observations. It could be shown that problematic biases of the coarser climate models are reduced if, as is usual in weather models, one switches to smaller grid-box sizes and improved descriptions of the cloud processes.

1 Introduction

Clouds are very effective in cooling the Earth. Clouds scatter sunlight back to space before it can be absorbed by the Earth's surface. They also trap longwave radiation originating from the warm surface and thus induce a counter-acting greenhouse effect (Ramanathan et al., 1989). In the global mean, the shortwave effect of clouds ($46 - 48 \text{ Wm}^{-2}$) dominates over their longwave effect ($26 - 28 \text{ Wm}^{-2}$) in the top-of-the-atmosphere (TOA) radiation budget, leading to a net negative cloud-radiative effect (CRE) of -18 to -20 Wm^{-2} (Arking, 1991; G. L. Stephens et al., 2012; Henderson et al., 2013; Zelinka et al., 2017). The magnitude of net radiative effects becomes even larger and more important for cloud systems over the mid-latitude oceans, where the net CRE is more than twice the global average (see e.g. Zelinka et al., 2017).

Cloud feedbacks, i.e. the impact of changes in clouds on the TOA radiation budget, remain a major source of uncertainty in future climate projections (Boucher et al.,

2013; Ceppi et al., 2017). Recent work indicates that the global-mean cloud feedback to global warming is likely positive, i.e., cloud changes will lead to an additional warming (Ceppi et al., 2017). This is largely attributed to a reduction in low-level cloud amount and a rise of high-level clouds (Zelinka et al., 2017). Yet, significant uncertainties remain in the parameterization of clouds and their radiative effects, in particular regarding the treatment of cloud microphysical processes in climate models (Gettelman & Sherwood, 2016). Understanding clouds and their radiative changes is also relevant for regional climate change, as the simulated response of the atmospheric circulation to global warming is strongly shaped by clouds (Voigt & Shaw, 2015; Voigt et al., 2019; Ceppi & Shepherd, 2017).

The steady increase in computational power and advent of a new generation of models that can harness this power has begun to allow for global atmospheric simulations with horizontal grid spacings on the order of a few kilometers (e.g. Satoh et al., 2018; Stevens et al., 2019). In these high-resolution simulations, clouds and the atmospheric flow interact much more naturally than in current low-resolution models typically run horizontal grid spacings of around 50 km. The explicit simulation of at least part of the cloud-scale circulations in fact provides a physical link between the resolved atmospheric flow and the parameterized cloud-microphysical processes (Satoh et al., 2019; Stevens et al., 2020). Moreover, and importantly, high-resolution models and satellite observations probe the atmosphere on similar spatial and temporal scales, allowing for a meaningful comparison between simulation and observations that helps model evaluation as well as the interpretation of observations (see also arguments from Satoh et al., 2019). As such, high-resolution modelling might break the so-called cloud parameterization "deadlock" (Randall et al., 2003) and promises to lead to more reliable simulations of cloud and precipitation responses to future climate change (Roberts et al., 2018; Collins et al., 2018; Stevens et al., 2020).

Motivated by these advances, we consider the radiative effects of mid-latitude cloud systems in simulations with a large range of horizontal resolutions, with three different treatments of atmospheric convection, and with two different treatments of cloud microphysics in this study. This creates a hierarchy of simulations that at the one end resembles current low-resolution climate models with parameterized convection and relatively simple cloud microphysics, and at the other end resembles the next-generation high-resolution models with explicit convection and more detailed cloud microphysics. Through this approach we investigate how a sequential reduction in model grid spacing from climate-model scales of 80 km down to 2.5 km affects, and hopefully improves, the simulation of cloud-radiative effects. Furthermore, we investigate the impact of subgrid-scale parameterization choices regarding convection (fully explicit convection vs. parameterized shallow convection vs. parameterized convection) and cloud microphysics (one-moment scheme vs. two-moment scheme) on cloud-radiative effects and the radiation budget. To this end we analyze simulations with the ICON (ICOsahedral Nonhydrostatic) model (Zängl et al., 2014) over a large domain of the North Atlantic. Our work contributes to recent efforts to understand the sensitivity of climate simulations with respect to horizontal resolution and convection parameterization (Webb et al., 2015; Haarsma et al., 2016; Evans et al., 2017; Maher et al., 2018; Thomas et al., 2018; Vanni ere et al., 2019). We expand these efforts by bridging the gap between current climate models and convection-permitting models.

The focus region of this study is the mid-latitude North Atlantic. This is motivated on the one hand side by its importance for current and future European weather, and on the other hand side by the difficulties of current coarse-resolution global climate models to represent the radiative effects of mid-latitude clouds (Bodas-Salcedo et al., 2014; Voigt et al., 2019) and their coupling to the circulation (Grise & Polvani, 2014). Cloud-radiative effects in the mid-latitudes feed back onto circulations. As such, they are essential to anticipated poleward shift and strengthening of the eddy-driven jet streams

121 under global warming (Voigt & Shaw, 2016; Albern et al., 2019; Ceppi & Hartmann, 2016;
 122 Li et al., 2019), and they also can impact mid-latitude weather on time-scales of days
 123 (Schäfer & Voigt, 2018; Grise et al., 2019)

124 Biases in simulated mid-latitude CREs appear to be primarily due to deficiencies
 125 in parameterized physics of clouds and convection (Ceppi & Hartmann, 2015). These physics
 126 strongly depend on cloud type. Analysis of data from space-born imaging radiometers
 127 has shown that low-level clouds over the oceans provide the largest contribution to the
 128 net TOA CREs because reflection of sunlight dominates over the trapping of longwave
 129 radiation (Hartmann et al., 1992; Ockert-Bell & Hartmann, 1992; Chen et al., 2000). The
 130 traditional cloud classification approaches have been revised to assess the importance
 131 of cloud regimes as a whole using clustering techniques (Oreopoulos & Rossow, 2011; Ore-
 132 opoulos et al., 2016; McDonald & Parsons, 2018) and the vertical structure of cloud fields
 133 based on active satellite sensors (G. Stephens et al., 2018; L’Ecuyer et al., 2019). The
 134 latter showed that clouds are predominantly organized in multiple layers, which is typ-
 135 ically not resolved by passive imagery. Because active satellite observations are very sparse
 136 in time and space, we here nevertheless rely on the traditional cloud classification ap-
 137 proach to separate cloud-cover and CRE model biases into contributions from different
 138 cloud types. The comparison is based on instantaneous and high-resolution geostation-
 139 ary satellite data. We follow modern model evaluation standards and sequentially de-
 140 rive synthetic satellite observations using a satellite simulator (similar to Bodas-Salcedo
 141 et al., 2011; Pincus et al., 2012) and cloud products with an advanced cloud classifica-
 142 tion software. For the latter step, we apply the cloud classification consistently for the
 143 full diurnal cycle (including nighttime). This improves the attribution of instantaneous
 144 CREs to different cloud types.

145 The paper is organized as follows: In section 2, the setup of the ICON model sim-
 146 ulations and sensitivity studies is described. Sect. 2 also provides information on the ob-
 147 served and synthetic narrow-band satellite radiances that are forwarded into the cloud
 148 classification software and on our method for deriving TOA radiation fluxes from Me-
 149 teosat observations. Sect. 3 presents the main results. We first consider domain-averaged
 150 radiation fluxes and CREs, and then split cloud cover and radiative effects into contri-
 151 butions from different cloud types. A summary and conclusions are given in section 4.
 152 A more detailed description of the modifications of the cloud classification software and
 153 supporting information is provided in the supplement.

154 **2 Data and Methods**

155 **2.1 Overview of the Analyses Workflow**

156 Before we provide more details, Fig. 1 presents an overview of the workflow and
 157 analyses steps for observations (black) and simulations (blue). The diagram is to be read
 158 from top to bottom. The input data from ICON (see Sect. 2.2) and Meteosat SEVIRI
 159 (see Sect. 2.3) are provided in the first row. From these, observed and simulated cloud
 160 types (Fig. 1a) and CREs (Fig. 1b) are derived, as shown in the last row. Importantly,
 161 this workflow makes sure that observations and simulations are directly comparable to
 162 each other.

163 For cloud classification, ICON simulations are translated into observation space us-
 164 ing the SynSat forward operator (Sect. 2.3). Based on observed and synthetic infrared
 165 brightness temperatures, cloud types are derived with the help of the NWCSAF v2013
 166 software (Sect. 2.5). For the assessment of CREs, Meteosat SEVIRI data are processed
 167 to obtain GERB-like allsky radiation fluxes at the top of the atmosphere (Sect. 2.4). The
 168 observed allsky fluxes are supplemented by simulated clearsky fluxes, which are corrected
 169 with a scaling factor in the shortwave and a constant additive offset in the longwave part
 170 to correct for biases in simulated ocean surface properties (Sect. 2.6).

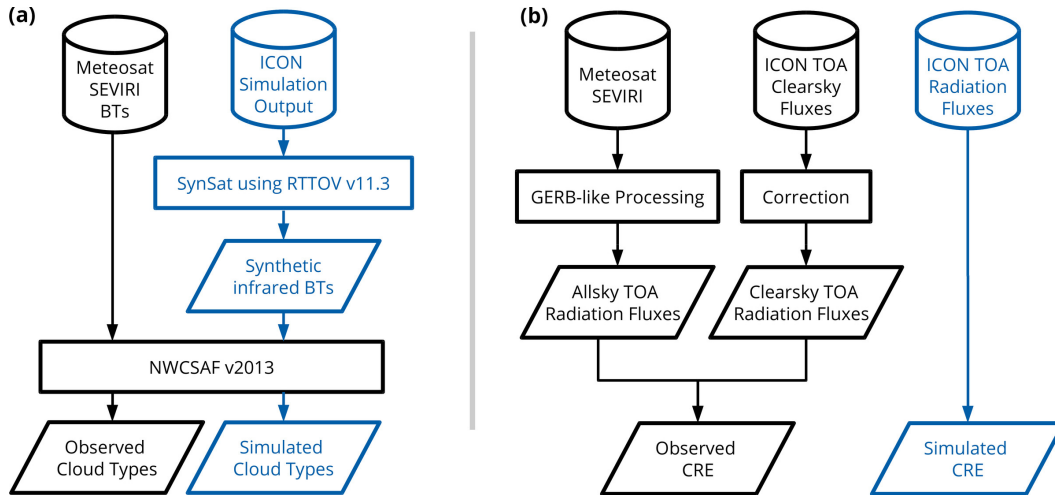


Figure 1. Overview of the workflow for (a) the calculation of a consistent cloud classification and (b) the derivation of CREs. Two parallel paths for observations (black) and the simulations (blue) are shown. The symbols in the top row visualize the input data (either satellite data archive or simulation output). Final data are shown in the last row. Rectangles denote processing methods further discussed in the text, and slanted parallelograms correspond to intermediate and final data.

171

2.2 ICON Simulations

172

173

174

175

176

177

178

179

180

181

182

183

184

185

186

187

188

We analyze simulations with the ICON model in limited-area setup performed over a large area of the North Atlantic (model version icon-2.1.00 with bug fixes for two-moment cloud microphysics). The simulation region extends from 78°W to 40°E in longitudinal direction, and from 23°N to 80°N in latitudinal direction (see Fig. 3 in Stevens et al. (2020)) and was chosen to encompass the region covered by the NAWDEX field campaign of fall 2016 (Schäfler et al., 2018). ICON is used with the numerical weather prediction physics package in a setup that largely follows the tropical Atlantic setup of Klocke et al. (2017). ICON is initialized from the integrated forecast system (IFS) analysis data of the European center for medium-range weather forecasts (ECMWF) at 0 UTC. The lateral boundary data are taken from IFS at 3-hourly resolution. At 0 UTC and 12 UTC IFS analysis data are used. In between 3-hr, 6-hr and 9-hr IFS forecast data are used. The continually updated analysis and forecast data ensure that the model stays close to the actual meteorology over the simulation period over several days (see below). The IFS data is retrieved at the highest available resolution in space (~ 9 km horizontal grid spacing). 11 days are analyzed in total. These result from 4 simulation sets that each cover a time span of 3 or 4 days, and for which the first day is disregarded as spin-up. The simulations are listed in Tab. 1.

189

190

191

192

193

194

195

196

197

198

The simulations are performed for six horizontal grid spacings of 80, 40, 20, 10, 5 and 2.5 km. In the vertical, always the same set of 75 levels is used. Sweeping through the horizontal resolution allows us to cover both the resolution of present-day global climate models, which typically run at 50-100 km, as well as the resolution of existing convection-permitting regional climate simulations (Prein et al., 2015) and upcoming global simulations (Stevens et al., 2019), which run at 2-5 km. For the finest resolution of 2.5 km the convection parameterization scheme is switched off either fully or partly. In the latter setup, only shallow convection is parameterized, whereas mid-level and deep convection are explicitly represented (ICON Model Tutorial April 2018). The setup with only shallow convection parameterization has emerged as the standard setup for 2.5km-ICON

Table 1. List of days simulated with ICON during the period of the NAWDEX field campaign in fall 2016. N_{sim} is the number of simulations as a result of testing for the sensitivity with respect to horizontal resolution and the treatment of cloud microphysics and convection.

	Simulation period	Analyzed days	N_{sim}
Set 1	Sep 20:0UTC - Sep23:0UTC	Sep 21, 22	14
Set 2	Sep 22:0UTC - Sep26:0UTC	Sep 23, 24, 25	20
Set 3	Sep 29:0UTC - Oct02:0UTC	Sep 30, Oct 01, 02	14
Set 4	Oct 02:0UTC - Oct06:0UTC	Oct 03, 04, 05	14

199 simulations at the German Weather Service (pers. comm. A. Seifert). For resolutions
 200 of 5 km and coarser, the convection scheme is fully enabled and takes care of shallow as
 201 well as mi-level and deep convection. In addition, for a three-day subset (Sep 22, 23, and
 202 24), the 2.5 km simulations are repeated with fully enabled convection parameterization,
 203 and the 5 and 10 km simulations with fully disabled convection parameterization. This
 204 allows us to compare the impact of the convection scheme with respect to changes in res-
 205 olution. Besides assessing the impact of resolution and representing convection in an ex-
 206 plicit or parameterized manner, we study the impact of representing cloud microphysics.
 207 To this end, all simulations are performed with the one-moment cloud microphysical scheme
 208 with graupel described in Baldauf et al. (2011) as well as with the two-moment cloud
 209 microphysical scheme of Seifert and Beheng (2006). The one-moment scheme is currently
 210 used operationally by the German Weather Service; the two-moment scheme is used in
 211 large-eddy mode simulations with ICON (Heinze et al., 2017).

212 To indicate the model setup in the plots and tables, the following nomenclature is
 213 used. For instance `ICON(10km, *, CP)` refers to ICON simulations with 10 km grid
 214 spacing, one-moment microphysics and fully enabled convection parameterization. In con-
 215 trast, `ICON(2.5km, **)` refers to ICON simulations with 2.5 km grid spacing, two-
 216 moment microphysics and fully disabled convection parameterization - a setup that is
 217 called "simulation with explicit convection" in the following. Lastly, `ICON(2.5km, **, sCP)`
 218 refers to a simulation in which only the shallow convection parameterization is
 219 enabled. Tab. 2 summarizes the model setups.

Table 2. Overview of different treatment of convection for the four sets of simulations (see Tab. 1). sCP means that only the shallow convection scheme is active. CP means that convection is fully parameterized. A notation example is given in the last row for simulations with 2.5 km grid spacing and one-moment cloud microphysics (indicated by *; two-moment cloud microphysics are indicated by **).

	explicit convection	sCP	CP
Set 1, 3, 4	2.5 km	2.5 km	5 - 80 km
Set 2	2.5, 5, 10 km	2.5 km	2.5 - 80 km
Notation example	<code>ICON(2.5km, *)</code>	<code>ICON(2.5km, *, sCP)</code>	<code>ICON(2.5km, *, CP)</code>

220 Radiative transfer is calculated by the global model version of the Rapid Radia-
 221 tion Transfer Model, RRTMG (Mlawer et al., 1997). RRTMG uses a reduced number
 222 of g-points for the correlated k-method to mitigate some of the computational burden
 223 of the parent RRTM model. 14 bands are used in the shortwave, 16 bands are used in
 224 the longwave. The solar constant is set to 1361.4 Wm^{-2} . For cloud overlap, the gener-

225 alized maximum-random overlap scheme of Hogan and Illingworth (2000) is used, with
 226 a vertical decorrelation length scale of 2 km. Ozone is specified according to the GEMS
 227 climatology, and aerosol according to the climatology of Tegen et al. (1997). Only aerosol-
 228 radiation-interactions are considered, aerosol-cloud interactions are not taken into ac-
 229 count. The cloud droplet number used in the radiation for the effective radius of droplets
 230 and crystals follows a prescribed vertical profile taken from the global atmosphere model
 231 ECHAM6 (Stevens et al., 2013). Cloud optical properties, i.e., single scattering albedo,
 232 extinction coefficient and asymmetry factor, are also specified as in ECHAM6. Radia-
 233 tion is called every 12 minutes. The radiation fields are output every hour and are al-
 234 ways consistent with the simulated cloud field, insolation, solar zenith angle and the state
 235 of the atmosphere and surface.

236 The diffuse ocean albedo is set to a constant value, $\alpha_{\text{dif}} = 0.07$. The direct ocean
 237 albedo follows the radiation scheme of Ritter and Geleyn (1992) and is a function of the
 238 diffuse albedo and the solar zenith angle, μ_0 ,

$$239 \quad \alpha_{\text{dir}} = \frac{1 + 0.5 \cos \mu_0 (\alpha_{\text{dif}}^{-1} - 1)}{(1 + \cos \mu_0 (\alpha_{\text{dif}}^{-1} - 1))^2}. \quad (1)$$

240 The maximum value allowed for α_{dir} is 0.999. Diffuse and the direct ocean albedo
 241 are independent of wavelength do not depend on surface roughness and wind speed.

242 Simulated radiation fluxes were re-gridded onto the observational grid (Sect. 2.3).
 243 Note that a common grid is important to accurately assess cloud-radiative effects because
 244 even small differences in the grid structure can induce artificial biases. For ICON sim-
 245 ulations with grid spacing of 2.5 and 5 km, re-gridding is done by means of box-averaging
 246 for which all model grid boxes that fall into the same observational grid box/pixel are
 247 averaged. For coarser ICON grids and for empty boxes at higher resolutions, re-gridding
 248 is done by means of a nearest-neighbor approach.

249 The analysis is restricted to ice-free ocean areas, which avoids complications from
 250 differences in surface albedo. As such, the analysis domain includes the North Atlantic
 251 and connected water bodies, including the North sea and the Baltic sea (see e.g. Fig. 2
 252 and Fig. 4). The southern boundary is at 28.3°N and is determined by the boundary nudg-
 253 ing zone of the 80 km grid. A maximum satellite zenith angle of 75° marks the north-
 254 ern boundary of the domain.

255 **2.3 Observed and Synthetic Meteosat Radiances**

256 Observations are provided by measurements of the imaging radiometer SEVIRI (Spin-
 257 ning Enhanced Visible and InfraRed Imager) on board the geostationary satellites of the
 258 Meteosat Second Generation (MSG) series operated by EUMETSAT (European Organ-
 259 isation for the Exploitation of Meteorological Satellites). SEVIRI provides satellite im-
 260 ages for 11 narrow-band channels covering solar and terrestrial radiation with a nadir
 261 resolution of $3 \times 3 \text{ km}^2$ and for one broad-band high-resolution visible channel with a three-
 262 fold higher horizontal resolution (Schmetz et al., 2002). For our study, we utilize data
 263 from SEVIRI's operational prime service located at a nominal longitude of zero degrees
 264 and a scan repeat cycle of 15 minutes. The temporal resolution is sub-sampled to hourly
 265 data to be comparable with the model output frequency. Due to the strategy of the SE-
 266 VIRI full disk scan which sequentially proceeds from South to North, a row-dependent
 267 time delay exists for the SEVIRI images. For the considered North Atlantic domain, the
 268 average delay is around 10 minutes between nominal and actual scan time. Hence, sim-
 269 ulated and observational data do not represent exactly the same instantaneous scenery
 270 - an aspect that is especially important for the downwelling shortwave radiation. In the
 271 next sections, Meteosat radiances are utilized to estimate instantaneous radiation fluxes,
 272 cloud cover and a classification into different cloud types.

273 An example of upwelling thermal radiation measured at $10.8\ \mu\text{m}$, is provided in Fig. 2
 274 (top row). The shown brightness temperatures (BTs) give measures of effective black-
 275 body temperatures depending on the temperature and emissivity of the medium. In the
 276 atmospheric window at $10.8\ \mu\text{m}$, atmospheric gases are relatively transparent and ther-
 277 mal emission mainly originates from the Earth surface, from clouds or from a combina-
 278 tion of the two (in case of semi-transparent or fractional clouds). High temperatures typ-
 279 ically represent clear regions, whereas low temperatures represent emission from high cir-
 280 rus clouds. In contrast, opacity of the moist atmosphere is significantly increased in the
 281 water-vapor channel at $6.2\ \mu\text{m}$ (see supplement for an example visualization). In cloud-
 282 free situations, most of the signal in the water-vapor channel originates from the upper
 283 troposphere between 200 to 300 hPa. Higher BT-values consequently mean lower effec-
 284 tive emission heights and thus reduced upper-level moisture. Surface and low to mid-
 285 level clouds are located at too low altitudes to be visible in the water-vapor images. How-
 286 ever, high cirrus does appear in addition to the upper-level water-vapor structures. In
 287 the scene of Fig. 2, a low-pressure system is located in the Atlantic ocean. Its frontal cloud
 288 system, seen by the low BTs, extends towards the south and approaches the British Is-
 289 lands. In the western part of this low-pressure system, cold and rather dry air is advected
 290 southwards. Marine, low-level clouds form within that cold sector and also propagate
 291 towards lower latitudes. Moist and dry-air patches are organized by synoptic-scale waves,
 292 sometimes leading to rather thin dry filaments.

293 For a fair comparison between observations and simulations, the simulated data
 294 have to be transformed into the observational space using forward operators (or some-
 295 times called instrument simulators). This has become a standard approach in the last
 296 decades (Morcrette, 1991; Roca et al., 1997; Chaboureau et al., 2000) and is especially
 297 important when such ambiguous variables like cloud cover and cloud types are taken into
 298 consideration (e.g. Pincus et al., 2012). For our study, we apply the so-called SynSat op-
 299 erator after Keil et al. (2006) and Senf and Deneke (2017) to derive synthetic satellite
 300 images with the sensor characteristics of MSG SEVIRI. The SynSat operator prepares
 301 vertical profiles of atmospheric temperature, humidity, condensate content and subgrid-
 302 scale cloud cover as well as several surface variables to perform single-column radiative
 303 transfer calculations with the RTTOV model (Saunders et al., 1999; Matricardi et al.,
 304 2004), here version 11.3. We apply a standard configuration that has been operationally
 305 employed by the German Weather Service for several years and utilized for ICON sim-
 306 ulations in previous studies (Heinze et al., 2017; Senf et al., 2018; Pscheidt et al., 2019).
 307 For this, diagnostic subgrid-scale cloud condensate content is added to its grid-scale coun-
 308 terpart, and ice and snow masses are simply combined to a frozen condensate content.
 309 Radiative properties of frozen condensate are estimated using relations for randomly-
 310 oriented hexagonal columns after Fu (1996) and McFarquhar et al. (2003). The deriva-
 311 tion of synthetic BTs is impacted by uncertainties in the formulation of microphysical
 312 and radiative hydrometeor properties. A complicating fact is that different model pa-
 313 rameterization handle hydrometeor properties differently leading to model-internal in-
 314 consistencies as additional cause for uncertainties in the forward calculations. Consid-
 315 ering these issues and typical parameter variations, Senf and Deneke (2017) showed that
 316 uncertainties in BTs are in the order of a few Kelvin and largest for semi-transparent
 317 cirrus clouds with low cloud-top temperatures and with emissivities close to 0.5.

318 Fig. 2 also provides a sequence of synthetic BTs for different model grid spacings
 319 from 2.5 to 80 km. As expected, the simulations capture the general cloud scenery and
 320 the synoptic-scale features very well. All simulations show the frontal cloud band that
 321 approaches the European continent and the upper-level trough located upstream in the
 322 North Atlantic. The coarser the resolution, the less detail can be seen in the synthetic
 323 BT-fields. However, no abrupt quality changes appear to happen with increased grid spac-
 324 ing.

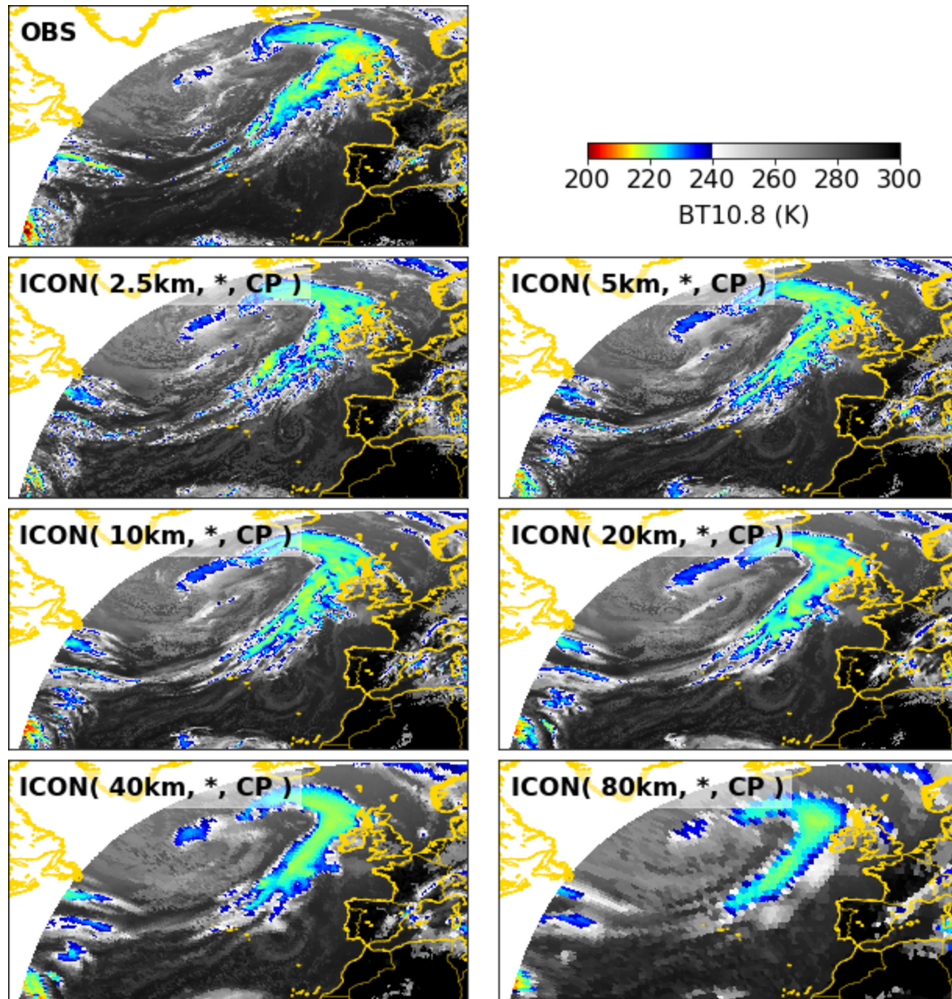


Figure 2. Overview of observed and simulated BTs from Meteosat SEVIRI's window channel at $10.8 \mu\text{m}$ for 1200 UTC 23 Sept 2016. Observations are compared to ICON simulations with increasing grid spacing (left to right and downwards, from 2.5 to 80 km). Only the subset of simulation experiments with one-moment microphysics and fully parameterized convection is chosen for visualization. A special color scheme is used to highlight observed and simulated features. BTs over land are also shown to improve anticipation of the cloud scenery. Further analysis however only considers the Atlantic ocean region.

325

2.4 Observations of Allsky Radiation Fluxes

326

327

328

329

330

331

332

333

The geostationary satellites of the Meteosat Second Generation series carry the broad-band radiometer GERB (Geostationary Earth Radiation Budget; Harries et al. (2005)). GERB provides accurate measurements of allsky TOA radiation fluxes. Unfortunately, during the period of our analysis GERB was in "safe mode" to protect its sensors. We therefore base our TOA radiation flux estimates on GERB-like products that are derived as internal products in the Royal Meteorological Institute of Belgium (RMIB) GERB processing system. The processing steps are in detail explained in Dewitte et al. (2008) and briefly summarized in the following.

334

335

The calculations of the GERB-like algorithm are based on multi-spectral observations from narrow-band SEVIRI channels as input. SEVIRI data are first calibrated to

336 correct for sensor aging and degradation (Meirink et al., 2013). Broadband filtered and
 337 unfiltered radiances are obtained from a narrow-to-broadband conversion method that
 338 relies on regression relations from a database of simulated scenes. To finally obtain ra-
 339 diation fluxes, angular distribution modelling (ADM) is applied. The longwave ADM is
 340 based on plane parallel radiative transfer (Clerbaux et al., 2003) and the same database
 341 as the narrow-to-broadband conversion. Thermal angular conversion factors depend on
 342 viewing zenith angle and SEVIRI’s thermal narrow-band observations. The shortwave
 343 ADMs are derived after Loeb et al. (2003) and also take into account cloud-optical prop-
 344 erties derived on each SEVIRI pixel. The ADMs are applied to spatial aggregates of 3
 345 $\times 3$ SEVIRI pixels. Previous work found that the accuracy of the narrowband-to-broadband
 346 conversion (GERB-like) is 3.5% for shortwave fluxes F_{sw} and 0.7% for longwave fluxes
 347 F_{lw} (Clerbaux et al., 2005). For a particular scene type, this error must be considered
 348 as a systematic error. For estimates of downwelling shortwave fluxes, temporal variations
 349 in the total solar irradiance are taken into account as described in Mekaoui and Dewitte
 350 (2008).

351 For our study, we retrieve GERB-like TOA radiation from the RMIB archive and
 352 regrid these to SEVIRI’s native resolution. Throughout the paper, we use a positive-upward
 353 convention so that upwelling fluxes are positive and downwelling fluxes are negative (following
 354 G. L. Stephens, 2005). This is typical for satellite studies. Model studies usually adopt
 355 the opposite positive-downward convention.

356 2.5 Cloud Classification

357 A cloud classification is derived from simulation and satellite data with the soft-
 358 ware of the satellite application facility in support to nowcasting and very short range
 359 forecasting (NWCSAF) version 2013. As input, the NWCSAF software expects multi-
 360 spectral data of MSG SEVIRI in its native data format. Using a set of several multi-spectral
 361 tests, a categorical classification is derived for all pixels classified as cloudy (Derrien &
 362 Le Gléau, 2005). The applied thresholds mainly depend on the illumination, the view-
 363 ing geometry, the geographical location and numerical forecast data describing the mois-
 364 ture and thermodynamic structure at coarser resolution. For the latter, short-term IFS
 365 forecasts are supplied.

366 Cloud types are mainly distinguished by their cloud-top height and opacity sim-
 367 ilar to the ISCCP-approach (International Satellite Cloud Climatology Project, see e.g.
 368 Rossow and Schiffer (1999)). No further distinction between convective and stratiform
 369 cloud structures is performed. The typical properties of the NWCSAF cloud types are
 370 shown in Fig. 3 and contrasted to the categorization after Hartmann et al. (1992). For
 371 practical reasons, we consider planetary albedo instead of cloud-optical thickness as mea-
 372 sure of cloud opacity. Clouds are divided into different height classes: very low, low, mid-
 373 level, high and very high clouds are approximately separated by the pressure levels of
 374 800, 650, 450 and 300 hPa. Cirrus clouds are distinguished by different opacity levels and
 375 called: semi-transparent (semi.) thin, semi. moderately thick, semi. thick cirrus as well
 376 as high and very high opaque clouds. The latter might also contain deep convective cores
 377 and parts of anvils close to upper-level convective outflow. An additional class is used
 378 for fractional clouds which are typically made of small boundary-layer cumuli. The sep-
 379 aration between this and the very-low cloud category is rather artificial. We therefore
 380 combine these two classes and end up with eight cloud types that will be utilized for fur-
 381 ther analysis. No undefined class exists, i.e. satellite pixels are either classified as cloud-
 382 free ($k = 0$) or cloudy ($k > 0$). Therefore, the total domain-average cloud cover can
 383 be estimated from the sum of fractions of the individual cloud types.

384 For very low / fractional clouds ($k = 1$ and $k = 9$ in Fig. 3), very low albedo
 385 values (close to the clearsky albedo of ~ 0.1) are most probable. This cloud type mainly
 386 consists of shallow clouds with low geometrical and optical thicknesses especially due to

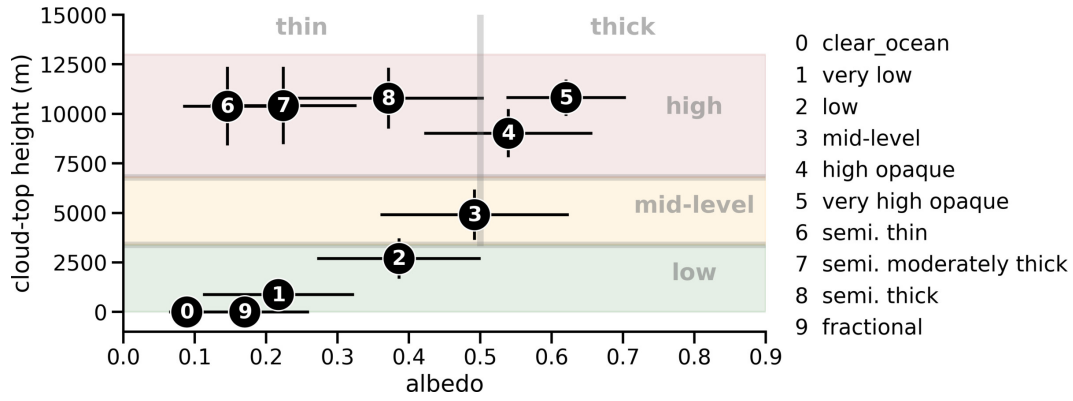


Figure 3. Planetary albedo versus cloud-top height for the different NWCSAF classes. The circles represent averages and the error bars give the standard deviation of clearsky or cloud properties. Data have been taken from the observed scenery shown in Fig. 2 and 4. Numbers $k = \{0 \dots 9\}$ refer to the different classes listed in the legend. Note that the cloud classes “fractional” and “very low” (which are shown separately here) are combined in the following analysis. For comparison, a second categorization after Hartmann et al. (1992) is provided as background image. It separates cloud amounts into three height categories (low, mid-level and high) as well as into two opacity levels (thin and thick clouds).

387 high sub-pixel variability and considerable clearsky contributions. For more opaque clouds
 388 with higher cloud tops, averaged albedo shifts to higher values. These cloud types have
 389 larger vertical and horizontal extent, and thus higher cloud-optical thicknesses. A sim-
 390 ilar shift to higher albedo values is found for semi-transparent cirrus going from semi.
 391 thin ($k = 6$) to semi. moderately thick ($k = 7$) to semi. thick ($k = 8$). Cloud-spatial
 392 structures and sub-pixel variability might be also an important factor for the albedo of
 393 semi-transparent cloud categories.

394 The NWCSAF software has undergone more than a decade of development and is
 395 highly adjusted to the needs of operational forecasters and nowcasting applications. It
 396 tries to account for as much information as available to derive a comprehensive and in-
 397 stantaneous classification of the cloud field. Changes in solar illumination can lead to
 398 changes in product quality and systematic differences, especially between day- and night-
 399 time, are inevitable in the standard setup of the NWCSAF cloud classification. To mit-
 400 igate these problems and to build a time-consistent cloud classification, we implemented
 401 a modification to the cloud product generation chain. The NWCSAF software has been
 402 set up to run in permanent-night conditions at which only infrared radiation of terres-
 403 trial origin is utilized. We developed an algorithm which reads in infrared SEVIRI ra-
 404 diances from a selected scene and thereafter outputs these data into a template valid for
 405 the same day, but for 0 UTC. The template files, including the embedded satellite ra-
 406 diances, are supplied to the NWCSAF software which generates a cloud classification in
 407 night-mode. To keep the software itself unmodified, we provide simple estimates of ra-
 408 diances at $3.9 \mu\text{m}$ which are mandatory, but contaminated with sunlight during day-time
 409 (further explained in the supplement). Beyond time consistency, there is an other ma-
 410 jor advantage of our approach: It also allows to exchange real observations with synthetic
 411 observations. In our case, we utilized synthetic radiances derived from all the different
 412 simulations with the SynSat method (see Sect. 2.3) and provide these data to the NWC-
 413 SAF software. In this way, a cloud classification is obtained for all simulations that is
 414 directly comparable to its observational counterpart.

415 An example scenery of an instantaneous and high-resolution cloud classification is
 416 shown in Fig. 4. The figure also illustrates the analysis domain, which is restricted to
 417 the subtropical and Northern mid-latitude parts of the Atlantic ocean. The scene is sim-
 418 ilar to the one shown in Fig. 2, but here the focus is on 2.5 km simulations with differ-
 419 ent treatment of convection and cloud microphysics. A frontal cloud band extends from
 420 the British Island to the open Atlantic. Upstream of this cold front, marine clouds of
 421 type "low" and "very low / fractional" propagate towards the European continent. In
 422 the subtropical areas, Meteosat observations show a rather low fraction of low and very
 423 low / fractional marine clouds. The amount of these cloud types, which appear in large
 424 patches of marine stratocumulus, is strongly overestimated in the simulations, especially
 425 in the variants with explicit convection.

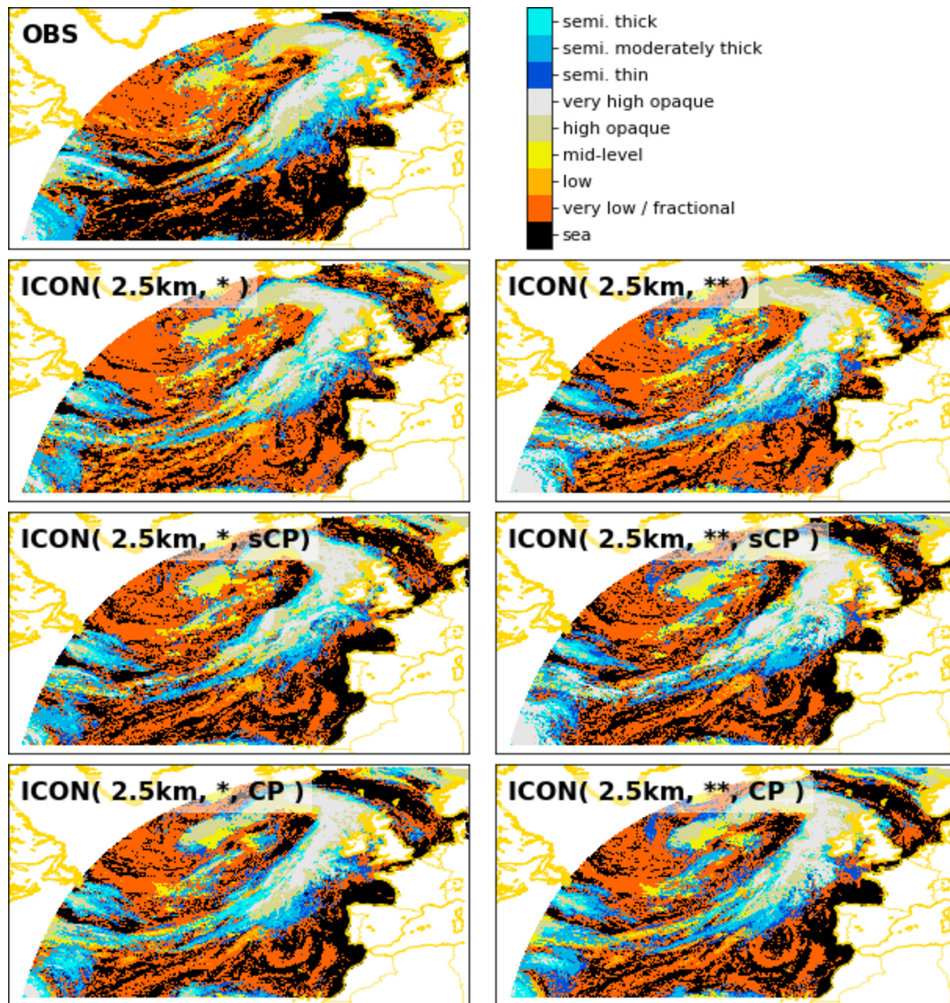


Figure 4. Example of observed and simulated cloud types for 1200 UTC 23 Sept 2016 as derived from Meteosat SEVIRI observations (top left) and ICON simulations with 2.5 km horizontal resolution. The left column is for simulations with one-moment cloud microphysics (*), the right column for simulations with two-moment microphysics (**). The second row is for fully explicit convection, the third row for simulations with a shallow convection scheme (sCP), and the fourth row for simulations with fully parameterized convection (CP).

426

2.6 Estimation of Observed Clearsky Radiation Fluxes

We are interested in the cloud impact on broadband shortwave and longwave radiation fluxes. This impact is commonly measured in terms of cloud-radiative effects (CREs),

$$\text{CRE}_{\text{net}} = \overline{F_{\text{net,clear}}} - \overline{F_{\text{net}}}, \quad (2)$$

427
428
429
430
431
432
433

which are defined as time-average difference between hypothetical clearsky fluxes that would occur in the absence of clouds and cloud-affected allsky fluxes. We follow the sign convention of G. L. Stephens (2005) and remind the reader that we defined upwelling allsky and clearsky fluxes as positive. Positive CREs indicate a gain of radiative energy and a warming effect of clouds, negative CREs indicate a loss of radiative energy and a cooling effect. Note that CREs are the net result of different cloud types; the radiative impact of individual cloud types is analyzed later in Sect. 3.2.

434
435
436
437
438
439
440

The ICON simulations provide allsky and clearsky fluxes, where the latter are calculated via a second radiation call with cloud fields set to zero. Simulated CREs follow directly from the application of eq. (2). As consequence, CREs are also available for regions that are classified as cloud-free ($k = 0$). These CREs are caused by undetected clouds. We thus need to distinguish between allsky and clearsky fluxes in cloud-free regions. Therefore, a distinction between “cloud-free” and “clearsky” is made thorough the rest of the paper.

441
442
443
444
445
446
447
448
449
450
451
452

The CREs of undetected clouds help us to assess the quality of the NWCSAF cloud detection (modified by us to run in night-mode). We discuss this effect first based on simulations (see Fig. 5). Please ignore the observational effects until we come back to them in the next paragraph. For a perfect cloud classification, all values should be at zero. This is not the case, however, and this demonstrates that a small amount of clouds remains undetected. Undetected clouds from the simulations contribute around 3 Wm^{-2} of additional shortwave reflection in cloud-free regions. In the longwave, simulated flux differences are between 1 and 2 Wm^{-2} in cloud-free regions and result from the reduced emission temperature of undetected clouds. The shortwave and longwave effects of undetected clouds partially cancel. When weighted by the clearsky fraction of around 25%, we conclude that CREs of undetected clouds have negligible impact on the total domain-average radiation budget.

453
454
455
456
457
458
459

Deriving clearsky fluxes is more difficult for the observations. Clearsky fluxes could be derived from satellite pixels classified as cloud-free, but even these might contain undetected clouds. For our analysis the situation is even more challenging because (i) the North Atlantic is very cloudy, and (ii) we are interested in instantaneous high-resolution radiation fluxes and CREs, for which the clearsky fluxes cannot be derived by temporal and spatial aggregation (as done in, e.g., Futyán and Russell (2005)). We therefore apply the following recipe to estimate observational clearsky fluxes (clearsky path in Fig. 1b):

460
461
462
463
464
465

- (i) Clearsky fluxes are taken from simulations as first guess (similar to Allan, 2011). The ICON(10km, *, CP) experiment has been chosen as reference, but any other simulation experiment or a combination of these would suffice as well.
- (ii) A bias correction is applied to simulated clearsky fluxes under the constraint that the *radiative effects of undetected clouds have similar magnitudes in observations and simulations*.

466
467
468
469
470

For the shortwave, $F_{\text{sw,up,clear}}$ has been rescaled by a factor of 0.88. From Fig. 6, we see that this scaling brings the simulated curve approximately down to the observational curve. In the longwave, an offset of 2 Wm^{-2} is subtracted from $F_{\text{lw,clear}}$. After correction, the simulated clearsky fluxes are used together with observed allsky fluxes for the calculation of observed CREs using eq. (2).

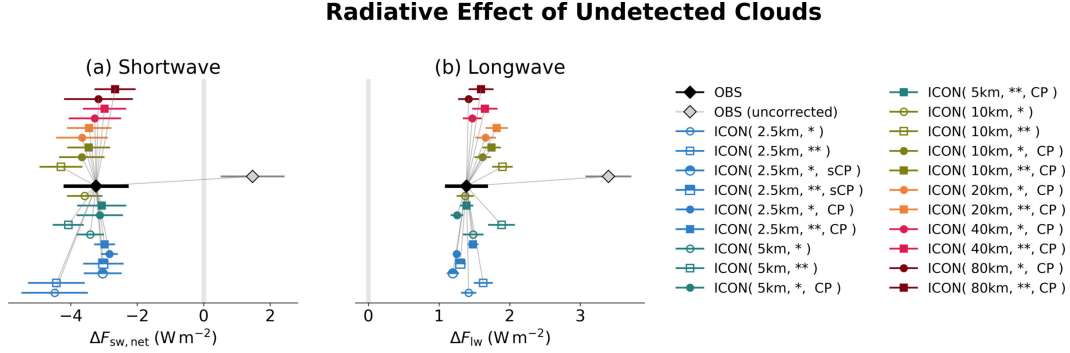


Figure 5. The radiative effect of undetected clouds in areas classified as cloud-free (i.e. $k = 0$). All data points show the average difference between clearsky and allsky fluxes for (a) shortwave $\Delta F_{sw} = F_{sw,clear} - F_{sw}$ and (b) longwave $\Delta F_{lw} = F_{lw,clear} - F_{lw}$. The bars give an robust estimate of the standard error of the daily-average values over all simulation sets, thus provide a confidence interval. For this, the difference between the 84-th and 16-th percentile has been calculated to approximate twice the multi-day standard deviation 2σ which was further divided by \sqrt{N} with $N = 11$. Colored symbols represent different simulations which have been vertically stacked to improve visibility. The gray symbols show the uncorrected observational estimate where the allsky fluxes are based on Meteosat, but the clearsky fluxes are directly taken from ICON(10km, *, CP). The black symbols show the corrected observational values with a scale factor applied to the shortwave and a constant additive offset to the longwave part of clearsky fluxes taken from ICON(10km, *, CP). Thin gray lines connect all other symbols to the observation for improved interpretation. The clearsky bias of the simulations is directly obtained from the difference between black and gray symbols.

471 The effects of the bias correction are illustrated in Fig. 5 where uncorrected observed
 472 CREs (gray symbols) are contrasted to corrected observed CREs (black symbols). The
 473 difference between the two is caused by biases in the simulated clearsky fluxes. Simu-
 474 lated shortwave fluxes are systematically too large in cloud-free regions. We believe this
 475 overestimation results from a too bright ocean surface albedo in ICON. Additional sup-
 476 port for this interpretation comes from independent internal investigations by the Ger-
 477 man Weather Service (pers. comm. A. Seifert). Moreover, simulated ocean surface seems
 478 to be too warm causing an overestimation of outgoing longwave clearsky fluxes that adds
 479 to the shortwave bias. In summary, we like to emphasize, that the applied strategy for
 480 cloud classification is extremely helpful to establish a consistent bias correction of instan-
 481 taneous clearsky fluxes estimated from simulations.

482 3 Results

483 3.1 Domain and Time-Averaged Radiation Fluxes and Cloud-Radiative 484 Effects

485 We begin with a comparison of observed and simulated radiation fluxes averaged
 486 over the North Atlantic domain and all days (Fig. 7). The observed net flux is around
 487 25 W m^{-2} and directed outward (Fig. 7a), implying that the North Atlantic region loses
 488 more radiative energy than it gains. All simulations show larger net fluxes, indicating
 489 that they overestimate the loss of radiative energy. Simulations with partly or fully pa-
 490 rameterized convection have a net flux of around 30 W m^{-2} , with the coarsest resolu-
 491 tion showing the smallest deviation with respect to observations. Furthermore, simula-

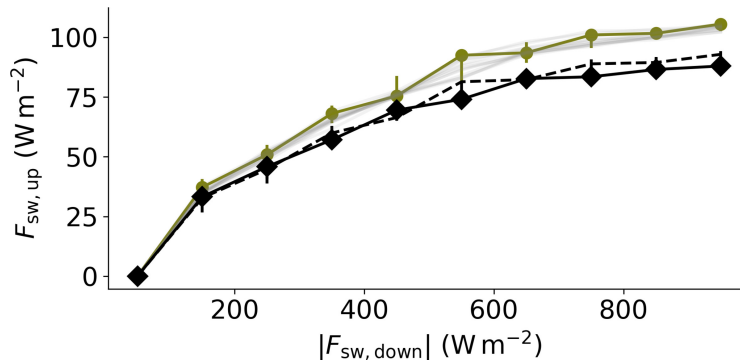


Figure 6. Simulated and observed upwelling versus downwelling shortwave fluxes in cloud-free areas. The upwelling flux is calculated for 10 bins of the downwelling flux. Symbols denote conditional median values and error bars show the inter-quartile range. Simulations are shown in gray, with the simulations for ICON(10km, *, CP) shown in green. Observations are shown by the black diamonds and the black solid line. The dashed black line shows the upwelling flux from ICON(10km, *, CP) rescaled by a factor of 0.88.

492 with fully parameterized convection have net fluxes slightly closer to the observa-
 493 tion when used with one-moment microphysics instead of two-moment microphysics. This
 494 might reflect previous model tuning that was done for one-moment but not for two-moment
 495 microphysics. Simulations with parameterized shallow convection show net fluxes very
 496 similar to simulations with fully parameterized convection. Much stronger deviations oc-
 497 cur, however, for simulations with explicit convection, for which the net flux reaches about
 498 40 W m^{-2} . We note that the deviations in the net flux are not simply a result of differ-
 499 ences in the downwelling shortwave flux, which amount to 1 W m^{-2} due to slight differ-
 500 ences in the solar constant in the simulations and observations.

501 The better agreement in terms of the net flux for low-resolution simulations and
 502 for simulations with (partly) parameterized convection results from compensating biases
 503 in outgoing longwave fluxes and upwelling shortwave fluxes, however (Fig. 7b and d). With
 504 one exception, the simulations overestimate outgoing longwave radiation (Fig. 7b), which
 505 corresponds to a too high effective emission temperature. The longwave bias increases
 506 with increasing grid spacing, with the largest bias found for the coarsest simulation at
 507 80 km resolution. Simulations with fully parameterized convection underestimate upwelling
 508 shortwave radiation, which corresponds to a too low planetary albedo. As for the long-
 509 wave bias, the shortwave bias is stronger for the coarser simulations. The better agree-
 510 ment in the net flux found for the coarser simulations is thus achieved for the wrong rea-
 511 son: a systematic bias compensation between longwave and shortwave fluxes that increases
 512 when a coarser resolution is used. Put differently, this also means that bias compensa-
 513 tion becomes smaller as the resolution is made finer - an encouraging signature of conver-
 514 gence with increasing resolution.

515 For the highest resolution simulations at 2.5 km the outgoing longwave flux improves
 516 when the shallow-convection scheme is disabled so that convection becomes fully explicit.
 517 This is in particular the case for two-moment microphysics, which agrees best with ob-
 518 servations in terms of the longwave flux (Fig. 7b). However, the simulations with fully
 519 explicit convection strongly overestimate the upwelling shortwave flux. As a result, the
 520 overall most satisfying agreement is found for simulations that combine two-moment mi-
 521 crophysics and parameterized shallow convection. The shallow-convection parameter-
 522 ization avoids the strong overestimation of upwelling shortwave flux found for fully ex-
 523 plicit convection.

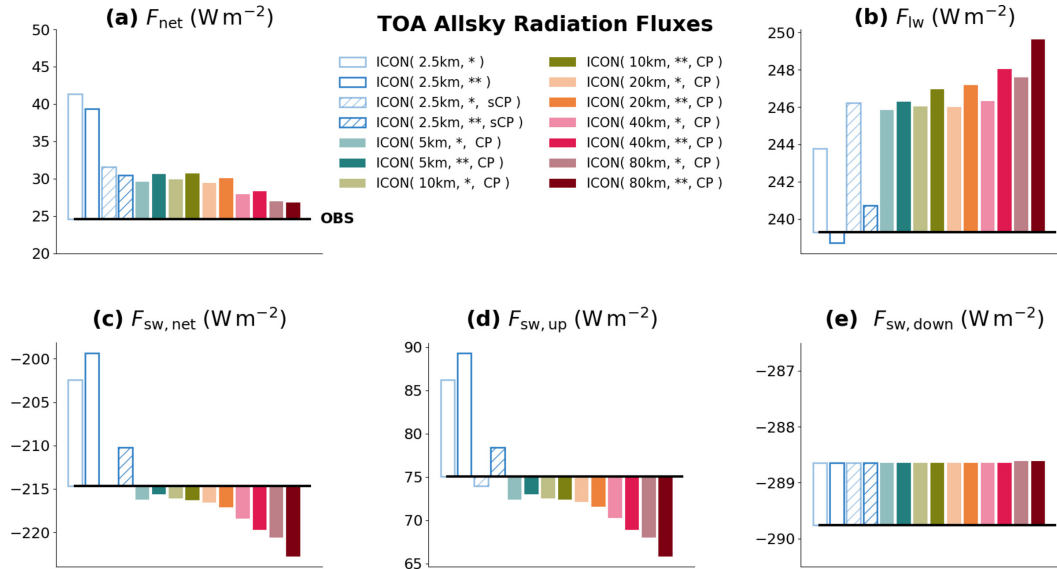


Figure 7. Domain and time-averaged allsky radiation fluxes: (a) total net flux, (b) outgoing longwave flux, (c) net shortwave flux, (d) upwelling shortwave flux, and (e) downwelling shortwave flux. Observations are shown by the black horizontal lines. The deviations of simulated fluxes with respect to observations are shown by colored bars.

524 The simulation of domain- and time-averaged CREs and cloud cover is analyzed
 525 in Fig. 8. For the observations, CREs are around -41 Wm^{-2} in the shortwave and around
 526 27 Wm^{-2} in the longwave, with a net cooling effect of clouds of -14 Wm^{-2} . Simulated
 527 shortwave and longwave CREs are negatively correlated, with larger positive longwave
 528 CREs obtained for more negative shortwave CREs (Fig. 8a). Simulations with fully param-
 529 eterized convection lie in the upper left quadrant of Fig. 8a and thus underestimate
 530 the magnitude of both longwave and shortwave CREs. Although these simulations show
 531 some improvement with decreasing grid spacing, none of the simulations approaches the
 532 observed CREs, and the impact of resolution appears to saturate at a grid spacing of 10 km.
 533 This indicates that even if the grid spacing was further reduced, the simulations would
 534 be unable to approach the observations if convection is fully parameterized. This idea
 535 is supported by Fig. S4 (supplementary material).

536 In contrast, simulations with shallow-convection scheme and fully explicit convec-
 537 tion are scattered around the observations (Fig. 8a). In these simulations, the impact
 538 of cloud microphysics is also much more pronounced. Overall, this suggests a clear ben-
 539 efit from (partly) disabling the convection scheme. In fact, simulations with shallow-convection
 540 scheme and two-moment microphysics show a remarkable match with observed longwave
 541 and shortwave CREs.

542 Fig. 8b-d further shows the relation between CREs and cloud cover. In the obser-
 543 vations, cloud cover is around 73%. Cloud cover is a primary control on CREs (e.g. Nam
 544 et al., 2012). Unsurprisingly this is visible in the simulations, which show a near-linear
 545 relation between cloud cover and the CREs. The observations, however, do not fall onto
 546 the simulation-based relationship. This leads to a dilemma: For none of the simulations
 547 do CREs and cloud cover at the same time match the observations. Cloud cover is bet-
 548 ter simulated for coarser grid spacings, whereas CREs improve as the grid spacing is re-
 549 fined. This indicates that work on cloud-radiative properties is needed.

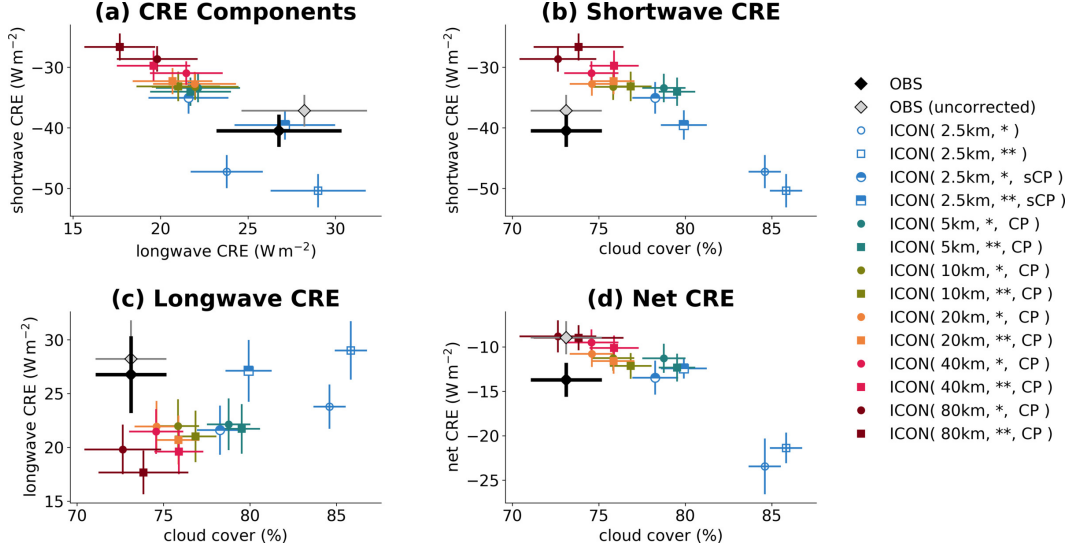


Figure 8. Comparison of domain- and time-averaged cloud-radiative effects and cloud cover: (a) longwave CRE vs. shortwave CRE. Cloud cover vs. (b) shortwave CRE, (c) longwave CRE, and (d) net CRE. Similar to Fig. 5, symbols denote average values and error bars provide confidence intervals. Please note the differences in the y-axis range.

Using Eq. (2) the radiation flux biases of the ICON simulations with respect to observations can be written as the sum of clearsky and CRE biases, i.e.,

$$\delta\bar{F} = \overline{F_{\text{ICON}}} - \overline{F_{\text{OBS}}} = \delta\overline{F_{\text{clear}}} - \delta\text{CRE}. \quad (3)$$

550 The results of this decomposition are collected in Fig. 9, with net flux biases shown in
 551 the left column, shortwave flux biases in the middle column, and longwave flux biases
 552 in the right column. The matrix presentation of Fig. 9 allows for two implicit summing
 553 rules: the left column is the sum of the middle and right columns, and the first row is
 554 the sum of 2nd and 3rd rows. The second row of Fig. 9 shows that net biases are to a
 555 substantial extent due to clearsky biases, which are independent of the simulation setup
 556 and amount to $\sim 7.4 \text{ Wm}^{-2}$. This explains why simulated clearsky fluxes could not be
 557 directly used as observational clearsky estimates and required a bias correction. The clearsky
 558 bias mostly arises from the shortwave ($\sim 5.6 \text{ Wm}^{-2}$), with a smaller longwave contri-
 559 bution ($\sim 1.8 \text{ Wm}^{-2}$). The magnitude of the clearsky shortwave bias is somewhat sur-
 560 prising, and likely reflects an imperfect representation of ocean surface albedo in the ICON
 561 simulations.

562 The dependence of allsky flux biases on resolution and the treatment of convection
 563 and cloud microphysics results entirely from CREs (Fig. 9, third row). The net CRE bias
 564 reduces the net allsky bias for simulations with fully parameterized convection, but in-
 565 creases it for simulations with fully explicit convection. For simulations with param-
 566 eterized shallow convection, the CRE biases depend on cloud microphysics. With one-moment
 567 microphysics, the CRE biases are similar to the biases found for fully parameterized con-
 568 vection. In contrast, with two-moment microphysics there is essentially no CRE bias,
 569 neither in the shortwave, longwave or net. The net flux bias of the two-moment simu-
 570 lation with parameterized shallow convection is therefore entirely due to clearsky biases,
 571 which could be decreased by adjusting the ocean albedo.

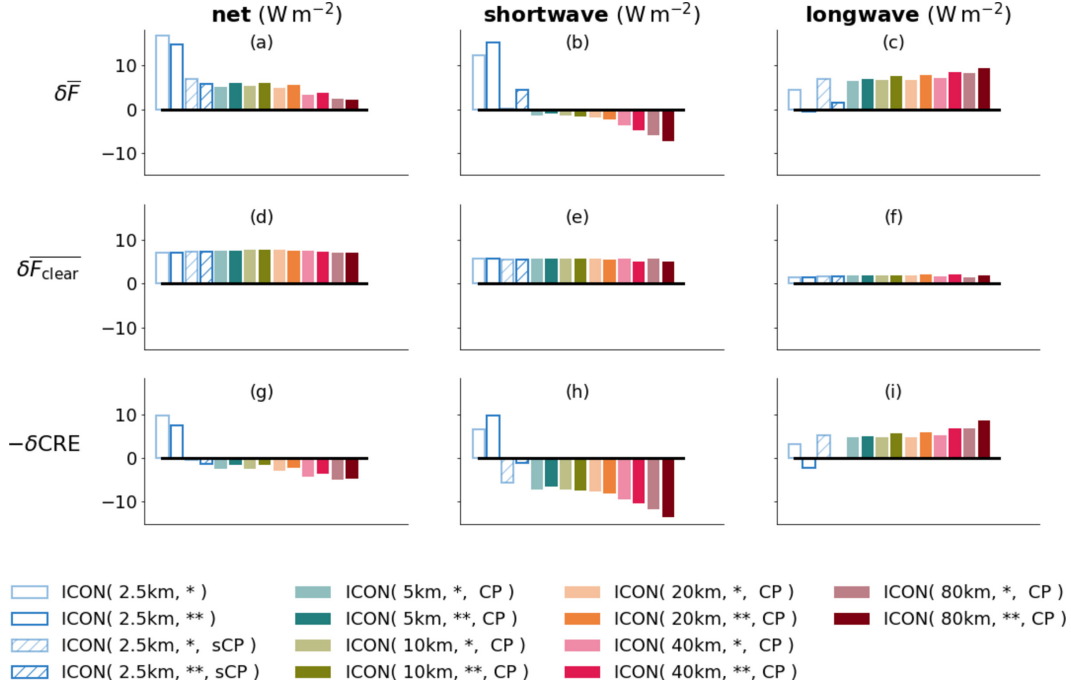


Figure 9. Decomposition of domain- and time-averaged biases for net (left), shortwave (middle) and outgoing longwave (right) radiation fluxes. The allsky bias (1st row) is the sum of clearsky (2nd row) and CRE (3rd row) biases. The clearsky biases are calculated with respect to the bias-corrected clearsky fluxes of ICON(10km, *, CP), which serves as observational reference.

572
573

3.2 Dependence of Cloud-Radiative Effects and Cloud Cover on Cloud Type

We now explore the origins of the domain- and time-averaged cloud-cover and CRE biases in the ICON simulations. To this end we use the cloud classification outlined in Sect. 2.5, which allows us to quantify the biases as a function of cloud type. This is done by writing the instantaneous domain-averaged net flux, F_{net} , as a sum of contributions from the K cloud types of the cloud classification,

$$F_{\text{net}} = \sum_{k=0}^K f_k F_{\text{net},k}, \quad (4)$$

where f_k is the fractional cloud cover of a certain cloud type k and $F_{\text{net},k}$ is the instantaneous net flux averaged over the area covered by cloud type k . Areas classified as cloud-free are included at $k = 0$. As before a positive sign is taken for upwelling fluxes. Instantaneous domain- and time-averaged CREs are decomposed analogously,

$$\text{CRE}_{\text{net}} = - \sum_{k=0}^K f_k \overline{(F_{\text{net},k} - F_{\text{net,clear},k})}, \quad (5)$$

574
575
576
577

where the cloud type-separated instantaneous net fluxes are averaged over time. This yields to a CRE decomposition into contributions from different cloud types. Note that clearsky and cloud-free fluxes are not equal, $F_{\text{net},0} \neq F_{\text{net,clear},0}$, because of clouds that are undetected by the cloud classification (cf. Fig. 5).

578
579

Fig. 10 presents the cloud-type separation of total cloud cover. In the observations, cloud cover is dominated by very low / fractional clouds, which contribute around 30%

580 to the total observed cloud cover of 73%. The three cloud types "low", "high opaque"
 581 and "semi. moderately thick" clouds each provide around 10%. The remaining cloud types
 582 are less important. From a qualitative point of view, all simulations capture the cloud
 583 cover of the different cloud types rather well. A few features of simulated cloud types,
 584 however, stand out:

- 585 (i) The cloud cover of very low / fractional clouds strongly depends on resolution and
 586 is better simulated in coarse-resolution simulations with grid spacings between 10
 587 and 80 km. Finer-resolution simulations substantially overestimate very low / frac-
 588 tional cloud cover, with a more severe overestimation as the grid spacing is decreased.
 589 The largest overestimation is found for simulations with explicit convection.
- 590 (ii) Most simulations underestimate the low cloud cover and overestimate the cloud
 591 cover of semi-transparent clouds. These biases are less resolution dependent and
 592 become smaller when convection is fully explicit.
- 593 (iii) The choice of the microphysics scheme (one-moment vs. two-moment scheme) has
 594 a dominant impact on the cloud cover of cirrus clouds, which are represented by
 595 the five cloud types "high" and "very high opaque" as well as "semi. thin", "semi.
 596 moderately thick" and "semi. thick". The effect is evident from high and very high
 597 opaque clouds, for which the two-moment scheme produces smaller cloud cover than
 598 the one-moment scheme for fully parameterized convection but higher cloud cover
 599 for very high opaque clouds and parameterized shallow convection. At the same
 600 time, the two-moment scheme leads to increased cloud cover and cloud-cover bi-
 601 ases for semi. thin and moderately thick clouds independent of the treatment of
 602 convection.

603 The domain- and time-averaged shortwave CRE depends on the typical albedo of
 604 a certain cloud type (see Fig. 3). This relation is further illustrated by Fig. 11a where
 605 CREs have been calculated for a hypothetical overcast situation in which the radiative
 606 effect of each cloud type was considered separately assuming a total coverage of 100%.
 607 Based on observations, very low / fractional clouds induce a rather low shortwave over-
 608 cast CRE of -30 Wm^{-2} . The shortwave overcast CRE increases reaching -140 Wm^{-2}
 609 for very high, opaque clouds. The concurrent increase of albedo and cloud-top height also
 610 leads to increases in longwave overcast CREs. The imperfect compensation between short-
 611 and longwave CREs causes net effects that have different signs for observed opaque and
 612 observed semi-transparent clouds. All opaque clouds induce a net cooling due to their
 613 negative net CREs in the observation. For observed low and mid-level clouds, the mag-
 614 nitudes of net overcast CREs are largest with -50 Wm^{-2} . The warming effect of ob-
 615 served semi-transparent clouds is less pronounced and is largest for semi. thick clouds
 616 with 15 Wm^{-2} .

617 The comparison of observed overcast CREs with their simulated counterparts helps
 618 to assess how good the different simulation setups represent the individual cloud-type
 619 specific radiation fluxes (independently of the fractional cloud cover of each type). On
 620 a qualitative level, all simulations perform very well showing the observed dependence
 621 of overcast CREs on cloud type. Most remarkably, none of the simulated semi-transparent
 622 cloud types causes significant positive net CREs (except for ICON(2.5 km, **, sCP)),
 623 i.e. hardly any of the ICON simulations induce a net domain-average warming from semi-
 624 transparent cirrus (see Fig. 11b). For all simulated semi-transparent cloud types, the long-
 625 wave CREs and thus their thermal cloud emissivities are underestimated (see Fig. 11a).

626 The dependence of allsky CREs on cloud type is presented in Fig. 11c-d. Follow-
 627 ing eq. (5), allsky CREs are calculated by weighting the difference between overcast and
 628 clearsky radiation fluxes by the cloud cover of each cloud type. The relative amount of
 629 each cloud type determines the importance of this cloud type and its CREs for the domain-
 630 and time-average. Thus, simulated biases in allsky CREs can arise from biases in (i) the
 631 radiative properties of a given cloud type, and (ii) the cloud cover of a given cloud type.

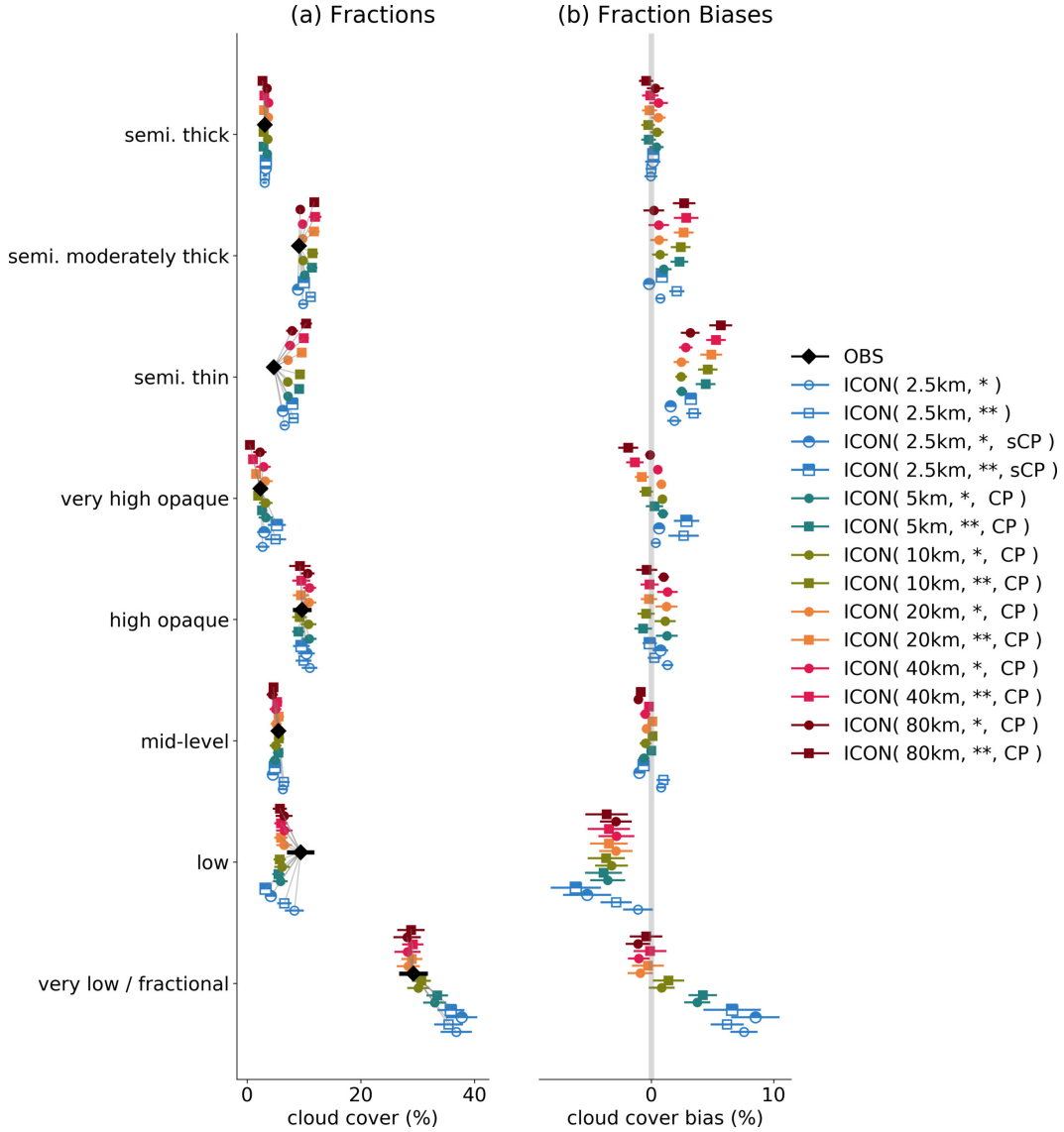


Figure 10. Observed and simulated cloud cover as a function of cloud type (a) as well as cloud cover biases of the simulations with respect to Meteosat observations (b). Similar to Fig. 5, symbols denote average values and error bars provide confidence intervals.

632 From Fig. 11d, we infer that mainly the four cloud types "very low / fractional", "low",
 633 "mid-level" and "high opaque" (with decreasing importance) contribute to the observed
 634 negative net allsky CREs. The remaining four cloud types either have near zero net allsky
 635 CREs or too little cloud cover. For simulations with fully parameterized convection,
 636 net allsky CREs for very low / fractional and low clouds are severely underestimated.
 637 The discrepancy is much reduced for simulations with shallow convection at 2.5 km grid
 638 spacing, especially for one-moment microphysics. In contrast, the net allsky CREs of very
 639 low / fractional clouds are overestimated in simulations with fully explicit convection.
 640 The allsky net CREs of mid-level clouds are better represented for simulations with ei-
 641 ther shallow or full convection scheme than in simulations with fully explicit convection.
 642 In addition, semi. moderately thick clouds have too negative allsky net CREs in all sim-
 643 ulations, with the largest bias for simulations with fully explicit convection.

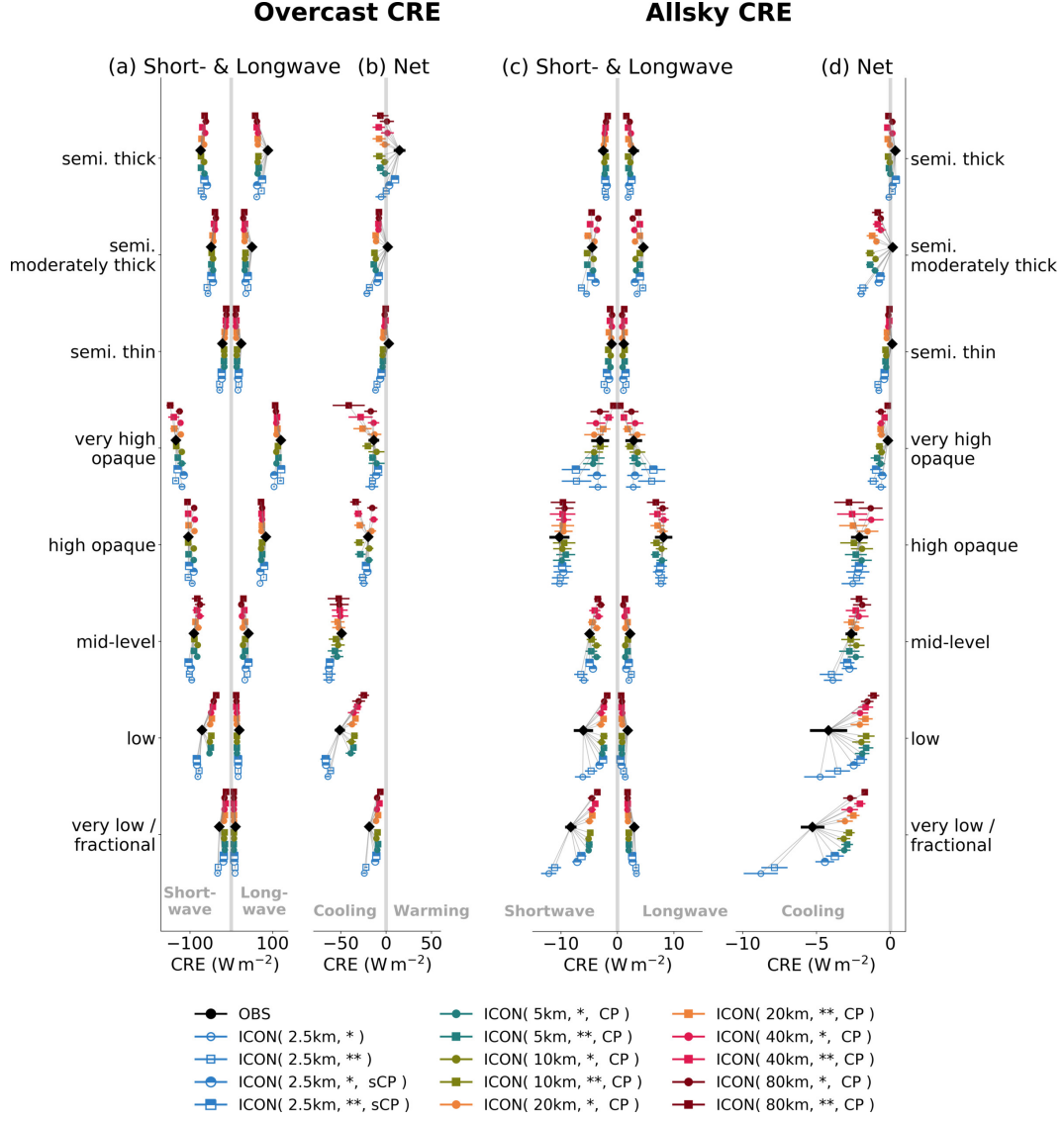


Figure 11. Observed and simulated (a,b) overcast CREs and (c,d) allsky CREs for different cloud types. Overcast CREs are calculated assuming a hypothetical cloud cover of 100%. Allsky CREs include weighting by the cloud-type’s specific cloud cover. Similar to Fig. 5, symbols denote average values and error bars provide confidence intervals.

To separate the effects of cloud type-dependent cloud cover and radiative properties on biases of simulated allsky CREs, we apply a bias decomposition to eq. (5),

$$\begin{aligned}
 \delta \text{CRE}_{\text{net}} = & - \underbrace{\sum_{k=0}^K \delta f_k (F_{\text{net},k} - F_{\text{net,clear},k})}_{\text{cloud cover}} - \underbrace{\sum_{k=0}^K f_k \delta (F_{\text{net},k} - F_{\text{net,clear},k})}_{\text{radiative properties}} \\
 & - \underbrace{\sum_{k=0}^K \delta f_k \delta (F_{\text{net},k} - F_{\text{net,clear},k})}_{\text{co-variation}}.
 \end{aligned} \tag{6}$$

644 The first term results from a misrepresentation of cloud cover, the second term from a
 645 misrepresentation of radiative properties and overcast CREs, and the third term from
 646 the co-variation between the two factors. As before, cloud-free contributions are included
 647 at $k = 0$. The decomposition holds for the allsky net CREs as well as its shortwave and
 648 longwave components.

649 Fig. 12 summarizes biases in the domain- and time-averaged CREs and their de-
 650 composition. As discussed in Sect. 3.1, net CREs are biased negative for simulations with
 651 explicit convection, i.e. clouds cool too much, but biased positive for simulations with
 652 shallow-convection scheme and fully parameterized convection (except for ICON(2.5km,
 653 *, sCP)), i.e. clouds cool too little. For the latter simulations, net CRE biases become
 654 smaller as the grid spacing is decreased. The compensation of CRE biases originating
 655 in the longwave and shortwave is very apparent for fully convection-parameterized sim-
 656 ulations (Fig. 12a-c).

657 The bias compensation between shortwave and longwave CREs leads to different
 658 roles of cloud cover and radiative properties, depending on whether one looks at net CREs
 659 or their shortwave and longwave components. For net CREs, cloud cover biases dom-
 660 inate. They are responsible for around half of the positive bias for fully parameterized
 661 convection (Fig. 12d). For simulations with fully explicit convection, in contrast, biases
 662 in radiative properties clearly control the net CRE biases. For the shortwave and long-
 663 wave CRE components, biases in radiative properties dominate in general. A pronounced
 664 compensation between shortwave and longwave CRE biases is apparent. We thus find
 665 that the earlier discussed compensation of shortwave and longwave flux biases directly
 666 traces back to a mis-representation of cloud-radiative properties. In all simulations ex-
 667 cept the ones with fully explicit convection, two-moment microphysics leads to less CRE
 668 biases due to radiative properties than the one-moment microphysics. The simulations
 669 with shallow-convection parameterization possess smaller biases than the fully param-
 670 eterized simulations. The simulations with fully explicit convection show acceptable re-
 671 sults for the longwave bias due to radiative properties. Their worse net performance orig-
 672 inates from the missing compensation by shortwave biases which are also negative for
 673 these simulations.

674 The interpretation of CRE biases is further supported by Fig. 13 which provides
 675 a detailed bias decomposition separated by cloud type. We see that not only the com-
 676 pensation between shortwave and longwave CRE biases is important, but also the com-
 677 pensation of biases originating from different cloud types. For the net CRE biases (Fig. 13c),
 678 mainly cloud types “very low / fractional” and “low” contribute to the positive bias of
 679 simulations with fully parameterized convection. This is partially compensated by a neg-
 680 ative net CRE bias from semi. moderately thick clouds. The net CRE bias of simula-
 681 tions with fully parameterized convection is again dominated by CRE biases due to ra-
 682 diative properties.

683 For shortwave and longwave CRE biases (Fig. 13a,b), it is found that the resolu-
 684 tion dependence of CRE biases not only originates from very low / fractional and low
 685 clouds, but also from very high opaque clouds. This cloud type is connected to deep con-
 686 vection which representation significantly improves for decreasing grid spacing. The sim-
 687 ulations with two-moment microphysics show a rather poor performance for the very high
 688 opaque clouds which needs to be addressed in future. In the shortwave, the positive CRE
 689 bias of simulations with fully parameterized convection comes mainly comes from very
 690 low / fractional and low clouds. For the former, biases in radiative properties dominate
 691 whereas for the latter CRE biases due to cloud cover also contribute. Switching from one-
 692 moment to two-moment scheme, we find improvements in the representation of short-
 693 wave components of individual radiative properties (see Fig. 12h and Fig. 13g) which are
 694 partially masked by worse cloud cover biases (see Fig. 12e). In the longwave, many cloud
 695 types simulated with fully parameterized convection show a negative bias originating from

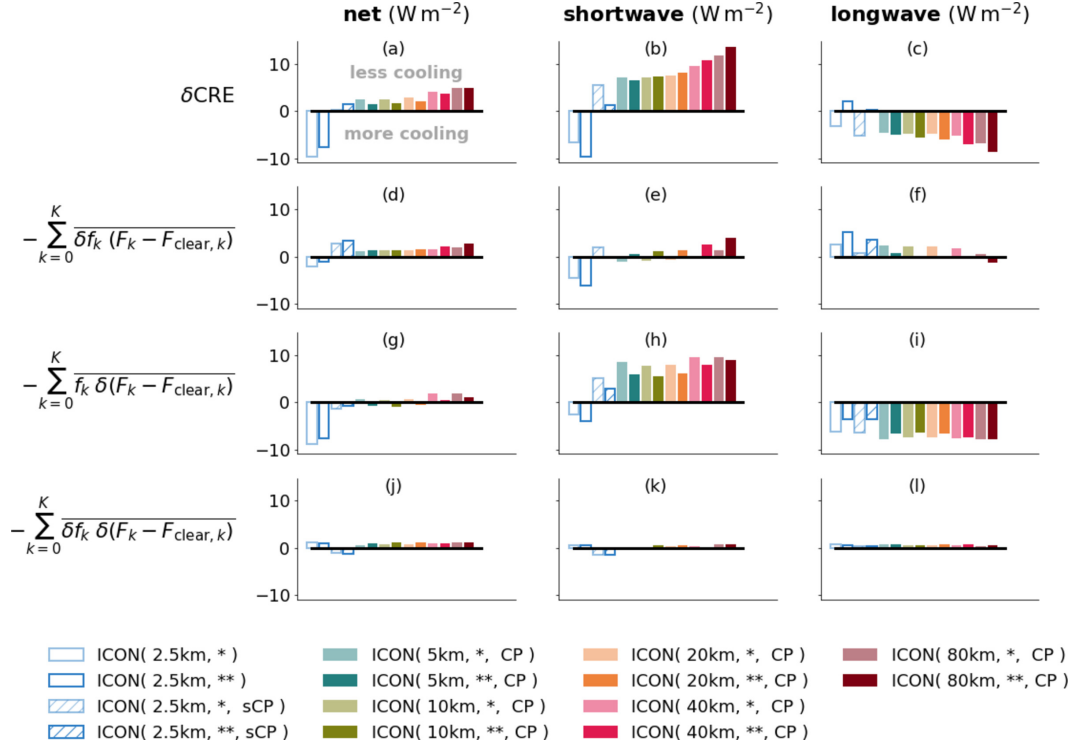


Figure 12. Decomposition of CRE biases (1st row) into contributions from biases in cloud cover (2nd row) and cloud-radiative properties (3rd row). Co-variations between biases in cloud cover and radiative properties are shown in the 4th row. The net CRE biases (left column) are decomposed into shortwave and longwave (right column) contributions.

696 the bias in radiative properties. The magnitudes of the individual longwave biases are
 697 much smaller for simulations with explicit convection.

698 In summary, the above analysis showed that future model development should equally
 699 concentrate on improvements of simulated clearsky and cloud-affected TOA radiation
 700 fluxes. For the former, we recommend to revise the formulation of ocean albedo to reach
 701 better consistency with observations. For CREs, strategies for further improvement depend
 702 on the choice of the convection scheme, especially at kilometer-scale resolutions.
 703 For simulations with fully parameterized convection, radiation is typically too weakly
 704 interacting with clouds, especially for low and very low / fractional clouds. Hence, improving
 705 radiative properties of these cloud types should be the main target in this model
 706 setup, either from a macrophysical or a microphysical point of view. Specifically, in the
 707 used ICON version the effective radius of cloud particles used for radiative transfer follows
 708 from a prescribed number concentration of cloud particles and is unaware of the number
 709 concentration simulated by the two-moment microphysics scheme. Adjusting this inconsistency
 710 might help to correct the negative biases in longwave CREs of semi-transparent cirrus.
 711 For simulations with only shallow or fully explicit convection, the radiative properties
 712 of clouds show signs of improvement. For these simulations, it becomes increasingly
 713 more important to constrain biases related to cloud cover, especially for cloud types
 714 “very low / fractional”, “low” and “very high opaque”.

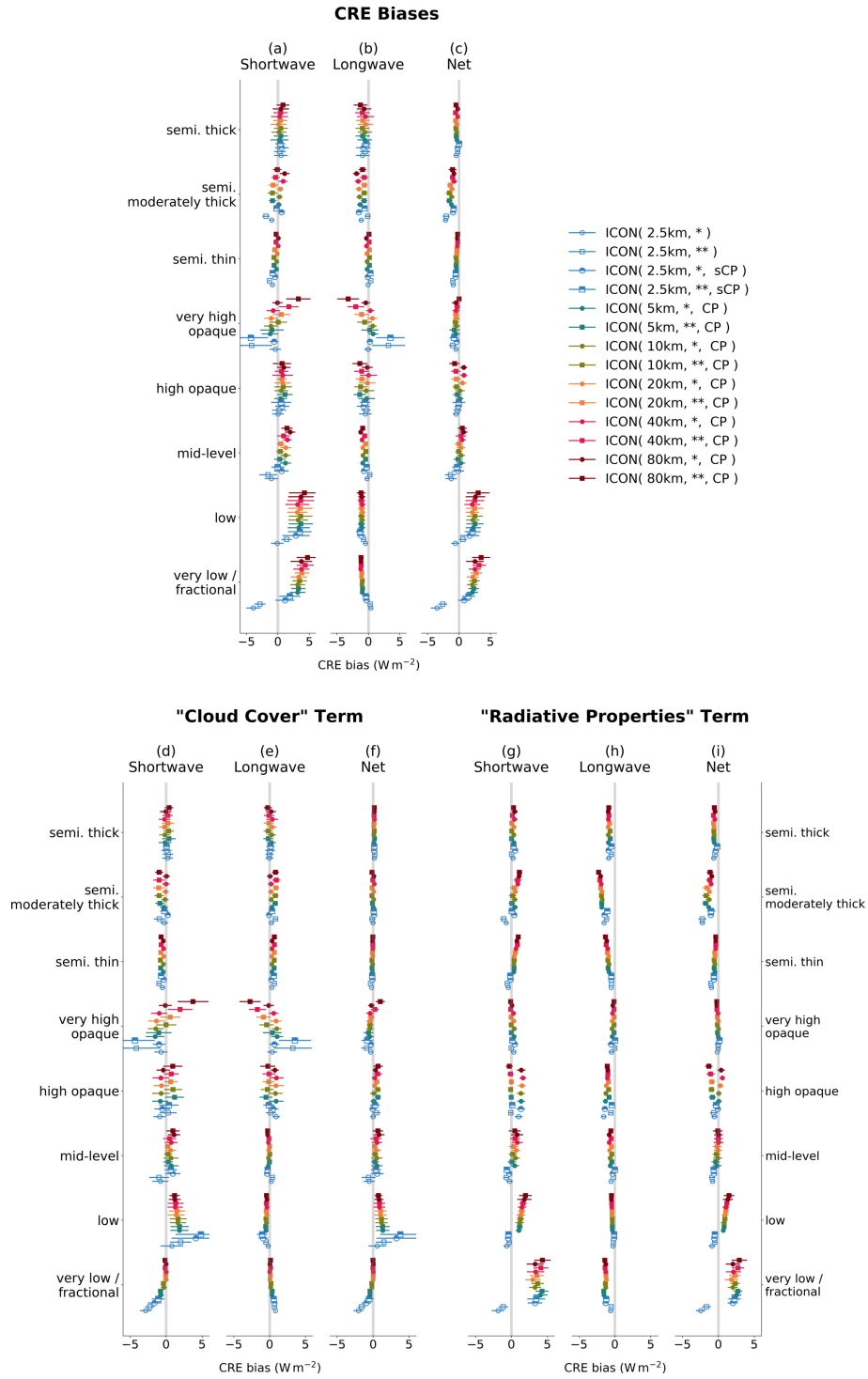


Figure 13. CRE biases and their decomposition for different cloud types. Following eq. (6), (top row) biases in CREs are separated into (bottom row) contribution from (left) cloud-cover biases and (right) radiation-flux biases. The split into (a, d, g) shortwave and (b, e, h) longwave components that sum up to the (c, f, i) net CRE bias is also provided in the different sub-panels. Similar to Fig. 5, symbols denote average values and error bars provide confidence intervals.

715 4 Conclusions and Outlook

716 Clouds regulate Earth’s energy budget (Ramanathan et al., 1989). Shallow low-
 717 level clouds are efficient scatterers of shortwave radiation and, in combination with their
 718 small thermal contrast to Earth’s surface, they have strong negative cloud-radiative ef-
 719 fects and cool the Earth. In contrast, the cloud-radiative effects of high-level cirrus clouds
 720 also include longwave effects so that depending on cirrus-optical properties these clouds
 721 can either have a near zero or a warming effect (G. L. Stephens, 2005).

722 In mid-latitude environments, cyclones lead to the formation of frontal cloud bands
 723 with a complicated mixture of stratiform and convective clouds, possibly including multi-
 724 layer structures and embedded convection. Realistically representing such complex cloud
 725 structures and their radiative effects poses a challenge to numerical models, especially
 726 over oceans where extended shallow boundary-layer cloud fields occur in addition. Fur-
 727 thermore, the radiative impact of clouds on the mid-latitude circulation might depend
 728 on cloud type. We therefore investigated the ability of a specific numerical weather pre-
 729 diction - the ICON model (Zängl et al., 2014) - to represent cloud cover and cloud-radiative
 730 effects for selected days of the NAWDEX field campaign in boreal autumn 2016 over a
 731 large North Atlantic domain. Using a comprehensive set of sensitivity simulations that
 732 vary horizontal grid spacing between 2.5 and 80 km, we identified sensitivities with re-
 733 spect to model resolution. Moreover, we studied the impact of different choices regard-
 734 ing the parameterization of cloud microphysics (one-moment versus two-moment scheme)
 735 and convection (fully parameterized, shallow-convection only, fully explicit). This allowed
 736 us to identify strengths and weaknesses of the different model setups, in particular with
 737 respect to top-of-atmosphere radiation fluxes and cloud-radiative effects.

738 To assess the ICON model we made use of multi-spectral observations from the geo-
 739 stationary Meteosat satellite in two ways. First, we analyzed observational estimates of
 740 instantaneous top-of-atmosphere radiation. Second, we derived a detailed and state-of-
 741 the-art cloud classification from the Meteosat observations. For a consistent compari-
 742 son between the ICON simulations and the observations, the simulation data were for-
 743 forwarded to a satellite forward operator performing radiative transfer calculations to de-
 744 rive synthetic infrared satellite images. This transfer of the simulations to observation
 745 space allowed us to subject simulations and observations to the same cloud classifica-
 746 tion software, and to analyze and compare observed and simulated cloud-type fields within
 747 the same framework.

748 In observations, the average net TOA radiation flux over the North Atlantic region
 749 and for the selected analysis days is around $+25 \text{ Wm}^{-2}$, indicating a net energy loss (re-
 750 member that we adopted a positive-upward convention for radiation fluxes). Clouds sub-
 751 stantially contribute to the energy loss and are responsible for a net cooling of -14 Wm^{-2} .
 752 Major contributors to the net CRE are shallow clouds of the cloud type "very low / frac-
 753 tional" and "low", which both contribute around -5 Wm^{-2} to the total net CRE. The
 754 shallow clouds also account for around half of the total cloud cover of 73%.

755 The main results of our comparison between observed and ICON simulated radi-
 756 ation fluxes and cloud fields are as follows:

- 757 (i) For all model setups, the domain- and time-averaged net TOA radiation flux is larger
 758 than in the observations, independent of resolution and the treatment of cloud mi-
 759 crophysics and convection. The ICON model thus overestimates the TOA loss of
 760 radiative energy. Simulations with fully parameterized convection underestimate
 761 TOA shortwave reflection and overestimate outgoing longwave radiation, i.e. seen
 762 from space they are too dark and too warm.
- 763 (ii) There is a systematic bias compensation between shortwave reflection and outgo-
 764 ing longwave radiation. The compensation is stronger for coarse-resolution simu-
 765 lations. Clearsky and CRE biases have similar magnitudes, but only CRE biases

- 766 are sensitive to horizontal resolution and in fact decrease with finer resolution. For
 767 fully parameterized-convection simulations, clouds are too weakly interacting with
 768 the radiation field leading to positive CRE biases in the shortwave and negative
 769 CRE biases in the longwave which partially compensate each other.
- 770 (iii) For none of the ICON setups, a simultaneous match between observed and sim-
 771 ulated CREs and total cloud cover is achieved. Cloud cover compares better to ob-
 772 servations for coarse resolutions, whereas CREs compares better to observations
 773 for finer resolutions.
- 774 (iv) The cloud cover of shallow clouds (types: “very low / fractional” and “low”) strongly
 775 depends on resolution. It compares well with observations for coarser resolutions
 776 of 10-80 km, but finer resolutions and explicit convection severely overestimate it
 777 by up to 50% relative to observations. For simulations with fully parameterized con-
 778 vection, net CRE-biases of shallow clouds are dominated by positive shortwave bi-
 779 ases in radiative properties. Biases in shortwave and net CREs are reduced when
 780 only shallow convection parameterization is applied. Using explicit convection even
 781 switches the sign of the shortwave CRE-biases leading to too bright shallow clouds
 782 and too large cloud-induced reflection.
- 783 (v) The choice of the microphysics scheme has dominant impact on cloud cover of cir-
 784 rus clouds leading to smaller cloud cover for high opaque and very high opaque clouds
 785 and larger cloud cover for semi. thin and semi. moderately thick clouds. No pro-
 786 nounced net warming effect is found for simulated semi-transparent clouds. The
 787 net CRE bias of semi-transparent clouds is negative and caused by a mis-representation
 788 of cirrus radiative properties, especially in the longwave.

789 In summary, our analysis shows that refining horizontal resolution and resolving
 790 convection allows the ICON model to more accurately represent cloud-radiative effects
 791 over the North Atlantic. We found substantial bias compensation between top-of-atmosphere
 792 shortwave and longwave radiation fluxes as well as between clearsky fluxes and cloud-
 793 radiative effects. An acceptable net performance of a selected model setup is not at all
 794 a guarantor of realistic individual contributions. The best representation of longwave and
 795 shortwave CREs is achieved when ICON is configured with two-moment cloud micro-
 796 physics, a shallow-convection scheme (explicit treatment of mid-level and deep convec-
 797 tion) and a horizontal resolution of 2.5 km.

798 The improvement from increasing resolution are gradually up to a resolution of 10 km,
 799 at which point a further increase in resolution no longer improves the simulated CREs.
 800 Instead, at resolutions of 10 km and finer, the improvement results from disabling the
 801 convection scheme so that the model is allowed to represent convection in an explicit man-
 802 ner. However, a resolution of 2.5 km is still too coarse to resolve the shallow clouds and
 803 circulation in the marine boundary layer, because of which the best simulation is achieved
 804 with an explicit treatment of mid-level and deep convection but a parameterized treat-
 805 ment of shallow convection. Compared to fully explicit convection, the use of a shallow-
 806 convection scheme mitigates the otherwise too high low-level cloud cover and too strong
 807 cloud shortwave reflection, and at the same time does not affect longwave CRE, which
 808 are dominated by high-level clouds.

809 Acknowledgments

810 FS and AV are supported by the German Ministry of Education and Research (BMBF)
 811 and FONa: Research for Sustainable Development (www.fona.de). This work contributes
 812 to the WCRP’s Grand Challenge on Clouds, Circulation, and Climate Sensitivity and
 813 the BMBF-funded project HD(CP)² : High Definition Clouds and Precipitation for Ad-
 814 vancing Climate Prediction. FS acknowledges funding under respective grants 01LK1507C
 815 and 01LK1503F, AV is supported under Grant Agreement 01LK1509A. The ICON sim-
 816 ulations were performed by AV at the DKRZ in Hamburg, Germany, which is thanked

817 for its support. We also thank EUMETSAT for producing the SEVIRI data, which have
818 been obtained from the TROPOS satellite data archive.

819 Concerning data availability: The GERB-like data is made freely available to the
820 user community via the RMIB OnLine Shortterm Service (ROLSS, see <ftp://gerb.oma.be>)
821 server, after registration. The primary data of the ICON simulations (run scripts, namelists,
822 scripts for lateral boundary data) will be published at KITopen of Karlsruhe Institute
823 of Technology.”

824 Open science: The analysis source code has been made freely available to improve
825 reproducibility of our results. Basic analysis tools are written in Python and published
826 at <http://doi.org/10.5281/zenodo.3657387>. The final plots for our paper were done with
827 Jupyter Notebooks which are hosted at [https://github.com/fsenf/nbook.CRE-2020-paper-](https://github.com/fsenf/nbook.CRE-2020-paper-plots)
828 plots.

829 References

- 830 Albern, N., Voigt, A., & Pinto, J. G. (2019). Cloud-radiative impact on the regional
831 responses of the midlatitude jet streams and storm tracks to global warming.
832 *J. Adv. Model. Earth Syst.*, *11*(7), 1940-1958.
- 833 Allan, R. P. (2011). Combining satellite data and models to estimate cloud radiative
834 effect at the surface and in the atmosphere. *Meteorological Applications*, *18*(3),
835 324-333.
- 836 Arking, A. (1991). The radiative effects of clouds and their impact on climate. *Bull.*
837 *Amer. Meteor. Soc.*, *72*(6), 795-814.
- 838 Baldauf, M., Seifert, A., Förstner, J., Majewski, D., Raschendorfer, M., & Rein-
839 hardt, T. (2011). Operational convective-scale numerical weather prediction
840 with the cosmo model: Description and sensitivities. *Mon. Wea. Rev.*, *139*(12),
841 3887-3905.
- 842 Bodas-Salcedo, A., Williams, K. D., Ringer, M. A., Beau, I., Cole, J. N. S.,
843 Dufresne, J. L., ... Yokohata, T. (2014, Jan). Origins of the Solar Radiation
844 Biases over the Southern Ocean in CFMIP2 Models*. *J. Climate*, *27*(1),
845 41-56. doi: 10.1175/JCLI-D-13-00169.1
- 846 Bodas-Salcedo, A., Webb, M. J., Bony, S., Chepfer, H., Dufresne, J.-L., Klein, S. A.,
847 ... et al. (2011). COSP: Satellite simulation software for model assessment.
848 *Bull. Amer. Meteor. Soc.*, *92*(8), 1023-1043.
- 849 Boucher, O., Randall, D., Artaxo, P., Bretherton, C., Feingold, G., Forster, P., ... et
850 al. (2013). Clouds and aerosols. In *Climate change 2013: The physical science*
851 *basis. contribution of working group i to the fifth assessment report of the in-*
852 *tergovernmental panel on climate change* (pp. 571–657). Cambridge University
853 Press.
- 854 Ceppi, P., Brient, F., Zelinka, M. D., & Hartmann, D. L. (2017). Cloud feedback
855 mechanisms and their representation in global climate models. *Wiley Interdis-*
856 *cip. Rev. Clim. Change*, *8*(4), e465.
- 857 Ceppi, P., & Hartmann, D. L. (2015). Connections between clouds, radiation, and
858 midlatitude dynamics: a review. *Curr. Clim. Change Rep.*, *1*(2), 94-102.
- 859 Ceppi, P., & Hartmann, D. L. (2016). Clouds and the atmospheric circulation re-
860 sponse to warming. *J. Climate*, *29*(2), 783-799.
- 861 Ceppi, P., & Shepherd, T. G. (2017, Nov). Contributions of Climate Feedbacks to
862 Changes in Atmospheric Circulation. *J. Climate*, *30*(22), 9097-9118. doi: 10
863 .1175/JCLI-D-17-0189.1
- 864 Chaboureaud, J.-P., Cammas, J.-P., Mascart, P., Pinty, J.-P., Claud, C., Roca, R.,
865 & Morcrette, J.-J. (2000). Evaluation of a cloud system life-cycle simulated
866 by the Meso-NH model during FASTEX using METEOSAT radiances and
867 TOVS-3I cloud retrievals. *Quart. J. Roy. Meteor. Soc.*, *126*(566), 1735-1750.

- 868 Chen, T., Rossow, W. B., & Zhang, Y. (2000). Radiative effects of cloud-type varia-
869 tions. *J. Climate*, *13*(1), 264-286.
- 870 Clerbaux, N., Bertrand, C., Caprion, D., Depaepe, B., Dewitte, S., Gonzalez, L., &
871 Ipe, A. (2005). Narrowband-to-broadband conversions for seviri. In *Proc. of*
872 *the 2005 eumetsat meteorological satellite conference* (p. 351-357).
- 873 Clerbaux, N., Dewitte, S., Gonzalez, L., Bertrand, C., Nicula, B., & Ipe, A. (2003).
874 Outgoing longwave flux estimation: improvement of angular modelling using
875 spectral information. *Remote Sens. Environ.*, *85*(3), 389 - 395.
- 876 Collins, M., Minobe, S., Barreiro, M., Bordoni, S., Kaspi, Y., Kuwano-Yoshida, A.,
877 ... others (2018). Challenges and opportunities for improved understanding of
878 regional climate dynamics. *Nature Climate Change*, *8*(2), 101.
- 879 Derrien, M., & Le Gléau, H. (2005). MSG/SEVIRI cloud mask and type
880 from SAFNWC. *Int. J. Remote Sens.*, *26*, 4707-4732. doi: 10.1080/
881 01431160500166128
- 882 Dewitte, S., Gonzalez, L., Clerbaux, N., Ipe, A., Bertrand, C., & Paepe, B. D.
883 (2008). The geostationary earth radiation budget edition 1 data processing
884 algorithms. *Adv. Space Res.*, *41*(11), 1906 - 1913.
- 885 Evans, S., Marchand, R., Ackerman, T., Donner, L., Golaz, J.-C., & Seman, C.
886 (2017). Diagnosing cloud biases in the gfdl am3 model with atmospheric
887 classification. *J. Geophys. Res. Atmos.*, *122*(23), 12,827-12,844.
- 888 Fu, Q. (1996). An Accurate Parameterization of the Solar Radiative Properties of
889 Cirrus Clouds for Climate Models. *J. Climate*, *9*, 2058-2082.
- 890 Futyan, J. M., & Russell, J. E. (2005). Developing clear-sky flux products for the
891 geostationary earth radiation budget experiment. *J. Appl. Meteor.*, *44*(9),
892 1361-1374.
- 893 Gettelman, A., & Sherwood, S. C. (2016). Processes responsible for cloud feedback.
894 *Curr. Clim. Change Rep.*, *2*(4), 179-189.
- 895 Grise, K. M., Medeiros, B., Benedict, J. J., & Olson, J. G. (2019). Investigating the
896 influence of cloud radiative effects on the extratropical storm tracks. *Geophys.*
897 *Res. Lett.*, *46*(13), 7700-7707.
- 898 Grise, K. M., & Polvani, L. M. (2014, Aug). Southern Hemisphere Cloud-Dynamics
899 Biases in CMIP5 Models and Their Implications for Climate Projections. *J.*
900 *Climate*, *27*(15), 6074-6092. doi: 10.1175/JCLI-D-14-00113.1
- 901 Haarsma, R. J., Roberts, M. J., Vidale, P. L., Senior, C. A., Bellucci, A., Bao, Q.,
902 ... von Storch, J.-S. (2016). High resolution model intercomparison project
903 (highresmip v1.0) for cmip6. *Geosci. Model Dev.*, *9*(11), 4185-4208.
- 904 Harries, J. E., Russell, J. E., Hanafin, J. A., Brindley, H., Futyan, J., Rufus, J., ...
905 Ringer, M. A. (2005). The geostationary earth radiation budget project. *Bull.*
906 *Amer. Meteor. Soc.*, *86*(7), 945-960.
- 907 Hartmann, D. L., Ockert-Bell, M. E., & Michelsen, M. L. (1992). The effect of cloud
908 type on earth's energy balance: Global analysis. *J. Climate*, *5*(11), 1281-1304.
- 909 Heinze, R., Dipankar, A., Carbajal Henken, C., Moseley, C., Sourdeval, O., Trömel,
910 S., ... Quaas, J. (2017). Large-eddy simulations over germany using ICON: a
911 comprehensive evaluation. *Quart. J. Roy. Meteor. Soc.*, *143*(702), 69-100.
- 912 Henderson, D. S., L'Ecuyer, T., Stephens, G., Partain, P., & Sekiguchi, M. (2013).
913 A multisensor perspective on the radiative impacts of clouds and aerosols. *J.*
914 *Appl. Meteor. Climatol.*, *52*(4), 853-871.
- 915 Hogan, R. J., & Illingworth, A. J. (2000). Deriving cloud overlap statistics from
916 radar. *Quart. J. Roy. Meteor. Soc.*, *126*(569), 2903-2909.
- 917 Keil, C., Tafferner, A., & Reinhardt, T. (2006). Synthetic satellite imagery in the
918 Lokal-Modell. *Atmos. Res.*, *82*, 19-25.
- 919 Klocke, D., Brueck, M., Hohenegger, C., & Stevens, B. (2017). Rediscovery of the
920 doldrums in storm-resolving simulations over the tropical Atlantic. *Nature*
921 *Geoscience*, *10*(12), 891-896.
- 922 L'Ecuyer, T. S., Hang, Y., Matus, A. V., & Wang, Z. (2019). Reassessing the effect

- of cloud type on earth's energy balance in the age of active spaceborne observations. part i: Top of atmosphere and surface. *J. Climate*, *32*(19), 6197-6217.
- Li, Y., Thompson, D. W. J., Bony, S., & Merlis, T. M. (2019, Feb). Thermodynamic Control on the Poleward Shift of the Extratropical Jet in Climate Change Simulations: The Role of Rising High Clouds and Their Radiative Effects. *J. Climate*, *32*(3), 917-934. doi: 10.1175/JCLI-D-18-0417.1
- Loeb, N. G., Manalo-Smith, N., Kato, S., Miller, W. F., Gupta, S. K., Minnis, P., & Wielicki, B. A. (2003). Angular distribution models for top-of-atmosphere radiative flux estimation from the clouds and the earth's radiant energy system instrument on the tropical rainfall measuring mission satellite. part i: Methodology. *J. Appl. Meteor.*, *42*(2), 240-265.
- Maher, P., Vallis, G. K., Sherwood, S. C., Webb, M. J., & Sansom, P. G. (2018). The impact of parameterized convection on climatological precipitation in atmospheric global climate models. *Geophys. Res. Lett.*, *45*(8), 3728-3736.
- Matricardi, M., Chevallier, F., Kelly, G., & Thépaut, J.-N. (2004). An improved general fast radiative transfer model for the assimilation of radiance observations. *Quart. J. Roy. Meteor. Soc.*, *130*, 153-173.
- McDonald, A. J., & Parsons, S. (2018). A comparison of cloud classification methodologies: Differences between cloud and dynamical regimes. *J. Geophys. Res. Atmos.*, *123*(19), 11,173-11,193.
- McFarquhar, G. M., Iacobellis, S., & Somerville, R. C. J. (2003). SCM Simulations of Tropical Ice Clouds Using Observationally Based Parameterizations of Microphysics. *J. Climate*, *16*(11), 1643-1664.
- Meirink, J. F., Roebeling, R. A., & Stammes, P. (2013). Inter-calibration of polar imager solar channels using seviri. *Atmos. Meas. Tech.*, *6*(9), 2495-2508.
- Mekaoui, S., & Dewitte, S. (2008). Total Solar Irradiance Measurement and Modelling during Cycle 23. *Sol. Phys.*, *247*(1), 203-216.
- Mlawer, E. J., Taubman, S. J., Brown, P. D., Iacono, M. J., & Clough, S. A. (1997). Radiative transfer for inhomogeneous atmospheres: RRTM, a validated correlated-k model for the longwave. *J. Geophys. Res. Atmos.*, *102*(D14), 16663-16682.
- Morcrette, J.-J. (1991). Evaluation of Model-generated Cloudiness: Satellite-observed and Model-generated Diurnal Variability of Brightness Temperature. *Mon. Wea. Rev.*, *119*(5), 1205-1224.
- Nam, C., Bony, S., Dufresne, J.-L., & Chepfer, H. (2012). The "too few, too bright" tropical low-cloud problem in cmip5 models. *Geophys. Res. Lett.*, *39*(21).
- Ockert-Bell, M. E., & Hartmann, D. L. (1992). The effect of cloud type on earth's energy balance: Results for selected regions. *J. Climate*, *5*(10), 1157-1171.
- Oreopoulos, L., Cho, N., Lee, D., & Kato, S. (2016). Radiative effects of global modis cloud regimes. *J. Geophys. Res. Atmos.*, *121*(5), 2299-2317.
- Oreopoulos, L., & Rossow, W. B. (2011). The cloud radiative effects of international satellite cloud climatology project weather states. *J. Geophys. Res. Atmos.*, *116*(D12).
- Pincus, R., Platnick, S., Ackerman, S. A., Hemler, R. S., & Patrick Hofmann, R. J. (2012). Reconciling simulated and observed views of clouds: Modis, isccp, and the limits of instrument simulators. *J. Climate*, *25*(13), 4699-4720.
- Prein, A. F., Langhans, W., Fossier, G., Ferrone, A., Ban, N., Goergen, K., ... Leung, R. (2015). A review on regional convection-permitting climate modeling: Demonstrations, prospects, and challenges. *Rev. Geophys.*, *53*(2), 323-361.
- Pscheidt, I., Senf, F., Heinze, R., Deneke, H., Trömel, S., & Hohenegger, C. (2019). How organized is deep convection over germany? *Quart. J. Roy. Meteor. Soc.*, *145*(723), 2366-2384.
- Ramanathan, V., Cess, R., Harrison, E., Minnis, P., Barkstrom, B., Ahmad, E., & Hartmann, D. (1989). Cloud-radiative forcing and climate: Results from the earth radiation budget experiment. *Science*, *243*(4887), 57-63.

- 978 Randall, D., Khairoutdinov, M., Arakawa, A., & Grabowski, W. (2003). Breaking
979 the cloud parameterization deadlock. *Bull. Amer. Meteor. Soc.*, *84*(11), 1547-
980 1564.
- 981 Ritter, B., & Geleyn, J.-F. (1992). A comprehensive radiation scheme for numerical
982 weather prediction models with potential applications in climate simulations.
983 *Mon. Wea. Rev.*, *120*(2), 303-325.
- 984 Roberts, M. J., Vidale, P. L., Senior, C., Hewitt, H. T., Bates, C., Berthou, S., ...
985 Wehner, M. F. (2018). The benefits of global high resolution for climate simu-
986 lation: Process understanding and the enabling of stakeholder decisions at the
987 regional scale. *Bull. Amer. Meteor. Soc.*, *99*(11), 2341-2359.
- 988 Roca, R., Picon, L., Desbois, M., Le Treut, H., & Morcrette, J.-J. (1997). Direct
989 comparison of meteosat water vapor channel data and general circulation
990 model results. *Geophys. Res. Lett.*, *24*(2), 147-150.
- 991 Rossow, W. B., & Schiffer, R. A. (1999). Advances in understanding clouds from is-
992 ccip. *Bull. Amer. Meteor. Soc.*, *80*(11), 2261-2287.
- 993 Satoh, M., Noda, A. T., Seiki, T., Chen, Y.-W., Kodama, C., Yamada, Y., ... Sato,
994 Y. (2018). Toward reduction of the uncertainties in climate sensitivity due to
995 cloud processes using a global non-hydrostatic atmospheric model. *Prog. Earth
996 Planet. Sci.*, *5*(1), 67.
- 997 Satoh, M., Stevens, B., Judt, F., Khairoutdinov, M., Lin, S.-J., Putman, W. M., &
998 Düben, P. (2019, 17). Global cloud-resolving models. *Curr. Clim. Change
999 Rep.*
- 1000 Saunders, R., Matricardi, M., & Brunel, P. (1999). An improved for assimilation
1001 of satellite radiance observations. *Quart. J. Roy. Meteor. Soc.*, *125*(556), 1407-
1002 1425.
- 1003 Schäfer, S. A. K., & Voigt, A. (2018, Mar). Radiation Weakens Idealized Mid-
1004 latitude Cyclones. *Geophys. Res. Lett.*, *45*(6), 2833-2841. doi: 10.1002/
1005 2017GL076726
- 1006 Schäfer, A., Craig, G., Wernli, H., Arbogast, P., Doyle, J. D., McTaggart-Cowan,
1007 R., ... Zinner, T. (2018). The north atlantic waveguide and downstream
1008 impact experiment. *Bull. Amer. Meteor. Soc.*, *99*(8), 1607-1637.
- 1009 Schmetz, J., Pili, P., Tjemkes, S., Just, D., Kerkmann, J., Rota, S., & Ratier, A.
1010 (2002). An introduction to Meteosat Second Generation (MSG). *Bull. Amer.
1011 Meteor. Soc.*, *83*(7), 977-992.
- 1012 Seifert, A., & Beheng, K. D. (2006, 01). A two-moment cloud microphysics param-
1013 eterization for mixed-phase clouds. part 1: Model description. *Meteor. Atmos.
1014 Phys.*, *92*(1), 45-66.
- 1015 Senf, F., & Deneke, H. (2017). Uncertainties in synthetic meteosat sevir infrared
1016 brightness temperatures in the presence of cirrus clouds and implications for
1017 evaluation of cloud microphysics. *Atmos. Res.*, *183*, 113-129.
- 1018 Senf, F., Klocke, D., & Brueck, M. (2018). Size-resolved evaluation of simulated
1019 deep tropical convection. *Mon. Wea. Rev.*, *146*(7), 2161-2182.
- 1020 Stephens, G., Winker, D., Pelon, J., Trepte, C., Vane, D., Yuhas, C., ... Lebsock,
1021 M. (2018). Cloudsat and calipso within the a-train: Ten years of actively
1022 observing the earth system. *Bull. Amer. Meteor. Soc.*, *99*(3), 569-581.
- 1023 Stephens, G. L. (2005). Cloud feedbacks in the climate system: A critical review. *J.
1024 Climate*, *18*(2), 237-273.
- 1025 Stephens, G. L., Li, J., Wild, M., Clayson, C. A., Loeb, N., Kato, S., ... Andrews,
1026 T. (2012). An update on earth s energy balance in light of the latest global
1027 observations. *Nat. Geosci.*, *5*(10), 691.
- 1028 Stevens, B., Acquistapace, C., Hansen, A., Heinze, R., Klinger, C., Klocke, D., ...
1029 others (2020). Large-eddy and storm resolving models for climate prediction
1030 the added value for clouds and precipitation. *accepted for J. Meteor. Soc.
1031 Japan.*
- 1032 Stevens, B., Giorgetta, M., Esch, M., Mauritsen, T., Crueger, T., Rast, S., ...

- 1033 Roeckner, E. (2013). Atmospheric component of the mpi-m earth system
1034 model: Echam6. *J. Adv. Model. Earth Syst.*, *5*(2), 146-172.
- 1035 Stevens, B., Satoh, M., Auger, L., Biercamp, J., Bretherton, C. S., Chen, X., ...
1036 Klocke, D. (2019). Dyamond: the dynamics of the atmospheric general cir-
1037 culation modeled on non-hydrostatic domains. *Prog. Earth Planet Sci.*, *6*(1),
1038 61.
- 1039 Tegen, I., Hollrig, P., Chin, M., Fung, I., Jacob, D., & Penner, J. (1997). Con-
1040 tribution of different aerosol species to the global aerosol extinction optical
1041 thickness: Estimates from model results. *J. Geophys. Res. Atmos.*, *102*(D20),
1042 23895-23915.
- 1043 Thomas, M. A., Devasthale, A., Koenigk, T., Wyser, K., Roberts, M., Roberts, C.,
1044 & Lohmann, K. (2018). A statistical and process oriented evaluation of cloud
1045 radiative effects in high resolution global models. *Geosci. Model Dev. Discuss.*,
1046 *2018*, 1–30. doi: 10.5194/gmd-2018-221
- 1047 Vannière, B., Demory, M.-E., Vidale, P. L., Schiemann, R., Roberts, M. J., Roberts,
1048 C. D., ... Senan, R. (2019). Multi-model evaluation of the sensitivity of
1049 the global energy budget and hydrological cycle to resolution. *Climate Dyn.*,
1050 *52*(11), 6817–6846.
- 1051 Voigt, A., Albern, N., & Papavasileiou, G. (2019, May). The Atmospheric Path-
1052 way of the Cloud-Radiative Impact on the Circulation Response to Global
1053 Warming: Important and Uncertain. *J. Climate*, *32*(10), 3051-3067. doi:
1054 10.1175/JCLI-D-18-0810.1
- 1055 Voigt, A., & Shaw, T. A. (2015, Feb). Circulation response to warming shaped by
1056 radiative changes of clouds and water vapour. *Nat. Geosci.*, *8*(2), 102-106. doi:
1057 10.1038/ngeo2345
- 1058 Voigt, A., & Shaw, T. A. (2016, Dec). Impact of Regional Atmospheric
1059 Cloud Radiative Changes on Shifts of the Extratropical Jet Stream in
1060 Response to Global Warming. *J. Climate*, *29*(23), 8399-8421. doi:
1061 10.1175/JCLI-D-16-0140.1
- 1062 Webb, M. J., Lock, A. P., Bretherton, C. S., Bony, S., Cole, J. N. S., Idelkadi, A., ...
1063 Zhao, M. (2015). The impact of parametrized convection on cloud feedback.
1064 *Phil. Trans. R. Soc. A*, *373*(2054), 20140414.
- 1065 Zängl, G., Reinert, D., Rípodas, P., & Baldauf, M. (2014). The ICon (ICosahedral
1066 non-hydrostatic) modelling framework of dwd and MPI-m: Description of the
1067 non-hydrostatic dynamical core. *Q.J.R. Meteorol. Soc.*, *141*(687), 563-579.
- 1068 Zelinka, M. D., Randall, D. A., Webb, M. J., & Klein, S. A. (2017). Clearing clouds
1069 of uncertainty. *Nature Climate Change*, *7*(10), 674.